NATIONAL TECHNICAL UNIVERSITY OF ATHENS

INTER-DEPARTMENTAL PROGRAM OF POSTGRADUATE STUDIES:

"MICROSYSTEMS & NANODEVICES"

Master Thesis:

MOLECULAR SIMULATIONS OF GRAPHENE-BASED MATERIALS FOR ORGANIC ELECTRONICS

Konstantinopoulos Stefanos

Supervisor:

Professor: Doros N. Theodorou

Athens

July 2017

NATIONAL TECHNICAL UNIVERSITY OF ATHENS

INTER-DEPARTMENTAL PROGRAM OF POSTGRADUATE STUDIES:

"MICROSYSTEMS & NANODEVICES"

Master Thesis:

MOLECULAR SIMULATIONS OF GRAPHENE-BASED MATERIALS FOR ORGANIC ELECTRONICS

Konstantinopoulos Stefanos

Verified by the examination committee on……………

D. N. Theodorou

Professor

School of Chemical Engineering

L. Tsetseris

Assoc. Professor

School of Applied Mathematics and Physical Sciences

C. Charitidis

Professor

School of Chemical Engineering

Athens

July 2017

Contents

Table of Figures

Abstract

Discotic Polycyclic Aromatic Hydrocarbons (PAHs) constitute a very promising class of materials for organic electronics applications. Its members can be considered as finite graphene flakes of nanometric dimensions. PAHs tend to self-assembly into molecular wires consisting of stacked disks. One dimensional hopping conductivity is manifested along the wire axis due to π-π interactions between polyaromatic cores. Furthermore, these disk-like molecules have the ability to accept around their periphery flexible groups that readily enhance their processability and properties, resulting in liquid crystalline behavior.

Hexa-peri-hexabenzocoronene (HBC) is a discotic molecule with hexagonal symmetry, consisting of 42 sp2 hybridized carbon atoms which form thirteen fused benzoic rings. Two analogous molecules with a more extended polyaromatic core are superphenalene ($C_{96}H_{24}$, C96) consisting of thirty four benzoic rings and bearing trigonal symmetry, and the $C_{132}H_{34}$ nanographene (C132) of tetragonal symmetry, made up of fifty rings. The aforementioned molecules can be regarded as the fusion product of three and four HBC molecules, respectively. In this study molecular systems grafted with hexane, dodecane and phytane side chains are examined by means of Molecular Mechanics (MM) and Molecular Dynamics (MD) simulations.

A series of discotics dimers corresponding to various symmetries have been brought to static equilibration via MM simulations for the determination of preferable stacking patterns. According to minimum energy dimeric states, initial configurations of molecular crystals are created. Structural and dynamical properties are examined by analyzing MD trajectories generated using the LAMMPS MD simulation software. State-of-the art integration algorithms and temperature and pressure control techniques have been utilized, alongside with sophisticated mesh-based techniques for handling long range interactions. As far as the potential energy surface of the systems is concerned, well validated force fields have been employed, which reproduce physical properties in good agreement with experimental findings.

The structure of supramolecular nanostructures of cylindrical form with core-shell characteristics is revealed utilizing principles of fiber diffraction. A methodology for the determination of theoretical X-ray Diffraction (XRD) spectra and 2-Dimensional Wide Angle X-ray Diffractograms (2D-WAXD) is presented. Complete structural characterization is carried out for soluble discotic systems focusing on the distance between aromatic cores, arrangement of molecular wires, and distribution of attached aliphatic side chains. XRD and 2D-WAXD patterns arising from equilibrated MD trajectories can be directly compared with available experimental data.

Περίληψη

Οι δισκόμορφοι πολυκυκλικοί αρωματικοί υδρογονάνθρακες αποτελούν μία πολλά υποσχόμενη κατηγορία υλικών για εφαρμογές ως ενεργά μέσα σε οργανικά ηλεκτρονικά. Παρουσιάζουν ομοιότητες σε μοριακό επίπεδο με νιφάδες γραφενίου νανομετρικών διαστάσεων. Οι πολυκυκλικοί αρωματικοί υδρογονάνθρακες έχουν την ιδιότητα να αυτό-οργανώνονται σε μοριακές ίνες. Λόγω των π-π αλληλεπιδράσεων μεταξύ των τροχιακών γειτονικών αρωματικών δίσκων, τα συστήματα αυτά εμφανίζουν μονοδιάστατη αγωγιμότητα κατά μήκος της αξονικής διεύθυνσης. Η δυνατότητα να επιδέχονται ευέλικτες πλευρικές ομάδες σε διάφορα σημεία της περιφέρειας, τους προσδίδει νέες ιδιότητες, όπως η ενεργοποίηση της υγροκρυσταλλικής συμπεριφοράς.

Τρία διαφορετικά είδη πολυκυκλικών αρωματικών υδρογονανθράκων μελετήθηκαν. Το εξα-περι-εξαβενζοκορονένιο (hexa-peri hexabenzocoronene – HBC) είναι ένα δισκόμορφο μόριο εξαγωνικής συμμετρίας το οποίο αποτελείται από 42 sp^2 υβριδισμένα άτομα άνθρακα τα οποία σχηματίζουν 13 βενζολικούς δακτυλίους. Το υπερφαινυλένιο ($C_{96}H_{24}$-C96) είναι ένα δισκόμορφο μόριο το οποίο παρουσιάζει τριγωνική συμμετρία και το $C_{132}H_{34}$ νανογραφένιο (C132) έχει τετραγωνική συμμετρία και δομείται από 50 δακτυλίους. Τα τελευταία δύο μόρια μπορούν να θεωρηθούν ως αποτέλεσμα σύνδεσης τριών και τεσσάρων μορίων HBC, αντίστοιχα. Στην παρούσα εργασία εξετάζονται μέσω προσομοιώσεων Μοριακής Μηχανικής και Μοριακής Δυναμικής νανογραφένια στην περιφέρεια των οποίων έχουν προσαρτηθεί αλειφατικές αλυσίδες κανονικού εξανίου, δωδεκανίου και φυτανίου και αυτοοργανώνονται σε μοριακούς κρυστάλλους.

Προκειμένου να καταστεί εφικτός ο προσδιορισμός των προτιμητέων τρόπων στοίβαξης μία πληθώρα από δισκόμορφα διμερή διαφορετικής συμμετρίας εξισορροπήθηκαν στατικά μέσω προσομοιώσεων Μοριακής Μηχανικής. Με βάση τους προτιμητέους τρόπους στοίβαξης των διμερών παράχθηκαν αρχικές απεικονίσεις μοριακών ινών, οι οποίες σχηματίζουν μοριακούς κρυστάλλους. Δομικές και δυναμικές ιδιότητες μοριακών συστημάτων νανογραφενίου υπολογίστηκαν από τροχιές Μοριακής Δυναμικής σε θερμοδυναμική ισορροπία, που προέκυψαν από τη χρήση του λογισμικού προσομοιώσεων LAMMPS. Η ολοκλήρωση των εξισώσεων κίνησης και ο έλεγχος της θερμοκρασίας και της πίεσης υλοποιήθηκε με τη χρήση σύγχρονων αλγορίθμων αιχμής, σε συνδυασμό με εξελιγμένες τεχνικές υπολογισμών στον αντίστροφο χώρο για την ποσοτικοποίηση των αλληλεπιδράσεων μακράς εμβέλειας. Για την ποσοτικοποίηση των αλληλεπιδράσεων χρησιμοποιήθηκαν εδραιωμένα πεδία δυνάμεων από τη βιβλιογραφία που αναπαράγουν ικανοποιητικά τα διαθέσιμα πειραματικά δεδομένα.

Στο δεύτερο κομμάτι της μεταπτυχιακής διπλωματικής εργασίας η δομή υπερμοριακών νανοδομών κυλινδρικής συμμετρίας με χαρακτηριστικά κελύφους-πυρήνα αποκαλύπτεται μέσω των αρχών που διέπουν την περίθλαση ακτίνων Χ. Υλοποιήθηκε μία καινοτόμα μεθοδολογία για τον προσδιορισμό φασμάτων περίθλασης ακτίνων Χ και δισδιάστατων διαγραμμάτων περίθλασης ευρείας γωνίας. Ο πλήρης δομικός χαρακτηρισμός πραγματοποιήθηκε για όλα τα συστήματα, εστιάζοντας στον υπολογισμό της απόστασης των πολυαρωματικών πυρήνων, τη διευθέτηση των μοριακών κιόνων καθώς και την κατανομή των πλευρικών αλειφατικών αλυσίδων. Τέλος, τα θεωρητικά διαγράμματα περίθλασης, τα οποία προέκυψαν από εξισορροπημένες τροχιές Μοριακής Δυναμικής, συγκρίθηκαν με πειραματικά διαγράμματα της βιβλιογραφίας.

Chapter 1: Introduction

1.1 Graphene based materials and organic electronics

Polycyclic aromatic hydrocarbons (PAHs) consist entirely of sp^2 hybridized carbon atoms and can be regarded as nanometric graphene flakes.[1,2] These molecules are excellent candidates for organic electronic applications such as organic light emitting diodes (o-LEDs), solar cells and field effect transistors (FETs).[3,4] Due to the interaction of neighboring delocalized *pi* molecular orbitals, semiconducting behavior via charge hopping mechanisms is manifested when such molecules are neatly packed.[4] A highly interesting characteristic of these molecules relies on their ability to host flexible side groups about their periphery via covalent functionalization. This peripheral alteration leads to high solubility in common organic solvents, thus prompting the use of "wet chemistry" methods for synthesis and processing towards the fabrication of organic electronic devices at much lower cost compared to traditional inorganic electronics[2].

Prototype discotic molecules with semiconducting properties are those consisting of fused phenyl rings, such as triphenylene, perylene and coronene[1,5] derivatives and more "exotic" molecules like metallomesogens from porphyrin and phtalocyanine groups and macrocyclic molecules based on phenylacetylene, alongside a plethora of other related aromatic molecules.[1]

After the peripheral covalent functionalization utilizing flexible side groups, such molecules gain enhanced spatial mobility and self-organize into molecular wires that, in turn, form symmetric molecular crystals. Semiconducting behavior is manifested via charge hopping along the axial direction of the formed molecular wires[1,2].

The current flagship discotic molecule for organic electronic applications is the hexa-peri-hexabenzocoronene (HBC), a molecule, with hexagonal symmetry, consisted of 42 sp^2 hybridized carbon atoms which form thirteen fused benzoic rings. Its dodecyl substituted variant (HBC-C12) exhibits in its crystalline form charge carrier mobility up to one third of graphite's hopping perpendicular mobility[5]. Also peripheral substitution enhances thermotropic behavior and increases solubility[2]. A special feature of HBC-C12 is the manifestation of liquid crystalline behavior when heated above room temperature[6]. Liquid crystallinity is exhibited as en-masse sliding of molecular wires parallel to the axial direction, with the latter forming a hexagonal supramolecular lattice[7].

x

The fusion of even more benzoic rings leads to the formation of extended flat polyaromatic molecules with variable symmetry and size[2]. These structures can be considered as finite nanometric graphene segments that are formally referred to as nanographenes[8]. Some characteristics examples are those of superphenalene $C_{96}H_{24}$ (C96) consisting of thirty four benzoic rings and bearing trigonal symmetry[9] and the $C_{132}H_{34}$ (C132) nanographene of tetragonal symmetry, made up of fifty rings[2]. These molecules can be crudely regarded as the fusion product between three and four HBC molecules, respectively[10].When functionalized with aliphatic side chains, such as hexane (C6) dodecane (C12) and phytane ($C_{20}H_{42}$ or C16,4), adequate solubility is achieved that leads to the formation of molecular wires and – ultimately- crystals of hexagonal symmetry[10].The molecules under study and the peripheral aliphatic side chains are illustrated in Figure 1.
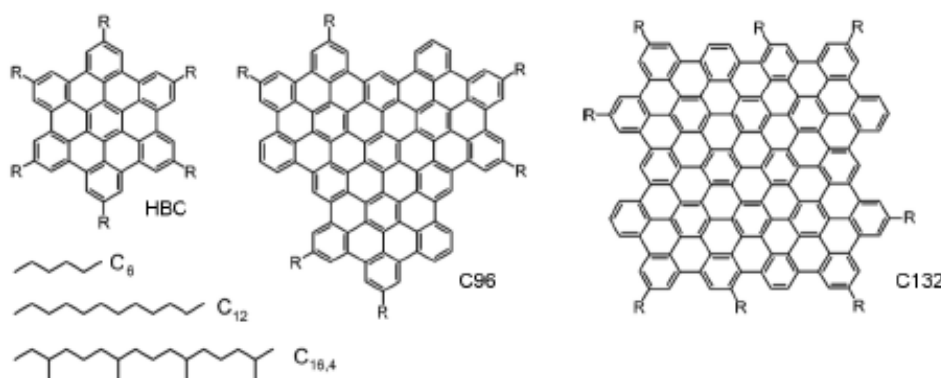
Figure 1: From left to right, a hexabenzocoronene (HBC), superphenalene (C96) and C132 molecule. On the left bottom of the figure, a n-hexane (C6), n-dodecane (C12) and a phytyl group (C16,4) are illustrated.

1.2. Aim and outline of thesis

The purpose of this study is dual. The first part is related to the computational study of HBC, C96 and C132 supramolecular assemblies. More precisely, an analysis from the level of molecular dimer, up to molecular wire and towards a molecular crystal is presented, utilizing Molecular Mechanics and Molecular Dynamics simulations. Furthermore, the studied systems constitute a prototype paradigm of supramolecular nanostructures of cylindrical form with core-shell characteristics. The stacked polyaromatic cores define a periodic axial core surrounded by a soft aliphatic nanophase. Structural and dynamical studies of such systems correspond to an interesting case study in the field of computational nanotechnology.

In the second part, the atomic structure of nanographene periodic molecular assemblies is examined. Initially, the theoretical background regarding the principles of diffraction is presented. The description begins from free electron scattering, arriving to a description of

fiber diffraction from the materials of interest. Theoretical X-Ray Diffraction (XRD) and Wide Angle X-ray Diffraction (WAXD) patterns arising from simulation trajectories are produced and compared with experimental data[10].

Chapter 2: Atomistic simulations of polycyclic aromatic hydrocarbons

2.1. Optimization schemes[11]

For a given function, *f,* that depends on one or more independent variables, the aim of optimization techniques is to calculate the values of those variables for which *f* gains its maximum or minimum value. The minimization and maximization processes can be mutually regarded since determining the minimum of *f* can be treated as finding the maximum of *–f* and vice versa. The maximum and minimum points can either be local or global. In general, the determination of global extrema is not a trivial task and two major heuristics are widely employed. The first method is related to the calculation of several local extrema from a variety of initial points and then selection of the most suitable. The second corresponds to perturbing a local extremum by a finite length and then seeing if the algorithm returns a different extremum. In general, the choice of the optimization algorithm depends on desired accuracy and memory storage requirement with respect to available computational resources.

Several optimization methods have been proposed for the one-dimensional case. These techniques may be divided into two main categories: optimization methods that require only the evaluation of the function and methods that also need the evaluation of derivatives. In the case of multidimensional functions the analog of a derivative is the gradient vector, which is expressed as:

$$\nabla f\left(x_1, x_2, ..., x_N\right) = \left(\frac{\partial f}{\partial x_1}, \frac{\partial f}{\partial x_2}, ..., \frac{\partial f}{\partial x_N}\right) \tag{2.1}$$

where *N* stands for the number of dimensions. Gradients may be calculated in an analytical manner or by taking finite differences of computed function values. Finally, a difference exists between algorithms that require storage of order *N* (e.g. conjugate gradient and steepest descent) and of those that require storage of order N^2 (e.g. quasi-Newton).

A brief description of the Steepest Descent method will be given here. The method starts from an initial point $\vec{P}_0$. Moving from point $\vec{P}_i$ to point $\vec{P}_{i+1}$ is achieved by minimizing along the line extending from $\vec{P}_1$ in the direction $-\nabla f\left(\vec{P}_1\right)$, which is the local downhill gradient. This method has the drawback that it requires many iterations for functions which have long valley surfaces. In this study, the Conjugate Gradient minimization scheme is used for minimizing the potential energy surface and therefore this method will be presented in more detail in the following section.

2.1.1. Conjugate Directions[11]

For a particular point $\vec{P}$ the function can be approximated by its Taylor series as a convex quadratic form:

$$f(\vec{x}) = f(\vec{P}) + \sum_i \frac{\partial f}{\partial x_i} x_i + \frac{1}{2} \sum_{i,j} \frac{\partial^2 f}{\partial x_i \partial x_j} x_i x_j \Rightarrow$$
$$f(\vec{x}) \approx c - \vec{b} \cdot \vec{x} + \frac{1}{2} \vec{x} \cdot \underline{\underline{A}} \cdot \vec{x} \tag{2.2}$$

where

$$c \equiv f(\vec{P}), \vec{b} \equiv -\nabla f|_{\vec{P}}, \left[\underline{\underline{A}}\right]_{i,j} = \frac{\partial^2 f}{\partial x_i \partial x_j}\bigg|_{\vec{P}} \tag{2.3}$$

The matrix $\left[\underline{\underline{A}}\right]_{i,j}$ is called the Hessian matrix and its components are the second partial derivatives of function $f(\vec{x})$ at $\vec{P}$. The gradient of $f(\vec{x})$ can be calculated as

$$\nabla f(\vec{x}) = \underline{\underline{A}} \cdot \vec{x} - \vec{b} \tag{2.4}$$

This implies that at a saddle point the gradient of the function will vanish and therefore the value of $\vec{x}$ will be obtained by solving:

$$\underline{\underline{A}} \cdot \vec{x} = \vec{b} \tag{2.5}$$

Moving towards a direction $\delta \vec{x}$, the gradient change can be calculated as

$$\delta(\nabla f) = \underline{\underline{A}} \cdot (\delta \vec{x}) \tag{2.6}$$

Consider minimizing a function along some direction $\vec{u}$. The function's gradient at the line minimum should be perpendicular to $\vec{u}$ at the line minimum. If the latter is not true, then there should be at least one nonzero directional derivative along $\vec{u}$. Now consider moving along a new direction $\vec{v}$. The condition that displacement along $\vec{v}$ does not spoil the minimization along $\vec{u}$, is that the change in gradient is perpendicular to $\vec{u}$. From equation 2.7 this is:

$$\vec{u} \cdot \delta(\nabla f) = \vec{u} \cdot \underline{\underline{A}} \cdot \vec{v} = 0 \tag{2.7}$$

When equation 2.7 holds for two vectors $\vec{u}$ and $\vec{v}$, they are said to be conjugate. In general, a conjugate set is a set of vectors such that the relation above holds pairwise for all its members. A function of quadratic form passing through N line minimizations (from a set of N linearly independent mutually conjugate vectors) will converge to a minimum. For functions that are not exactly quadratic, repeated cycles of N line minimizations will converge quadratically to the minimum.

2.1.2 The Conjugate Gradients minimization scheme [11,12]

The Conjugate Gradients algorithm is an iterative minimization method that calculates the least value of a differentiable function. This optimization scheme requires the calculation of first derivatives without having to resort to second derivatives. Let N be the number of variables of the objective function $f(\vec{x})$ and k represent the number of iterations.

For $k=1$ the steepest descent direction is defined as:

$$\vec{d}_k = -\vec{g}_k = -\vec{g}(\vec{x}_k) = -\nabla f(\vec{x}_k) \tag{2.8}$$

Otherwise, for $k>1$ the steepest descent direction is expressed as:

$$\vec{d}_k = -\vec{g}_k + \beta_k \vec{d}_{k-1} \tag{2.9}$$

where β_k is the fraction of gradients between two successive iterations:

$$\beta_k = \|\vec{g}_k\|^2 / \|\vec{g}_{k-1}\|^2 \tag{2.10}$$

with vector norm being Euclidean. The new iteration vector $\vec{x}_{k+1}$ is obtained searching the least value of $f(\vec{x})$ from $\vec{x}_k$ along the direction $\vec{d}_k$

$$\vec{x}_{k+1} = \vec{x}_k + \lambda_k \vec{d}_k \tag{2.11}$$

where λ_k is the value of λ that minimizes the one dimension function φ_k

$$\varphi_k(\lambda) = f(\vec{x}_k + \lambda \vec{d}_k) \tag{2.12}$$

At this point the iteration terminates and another one begins if $f(\vec{x}_{k+1})$ or $g(\vec{x}_{k+1})$ are not sufficiently small.

2.2 Molecular Dynamics [13–15]

Molecular Dynamics (MD) is a deterministic simulation method that computes the properties of a system consisting of many particles. MD methods reproduce properties on the microscopic level, like momentum and position of the particles and calculates macroscopic properties such as enthalpy, pressure, temperature etc.

Within a classical approach, particle trajectories are dictated by the potential energy surface of the system. In Cartesian coordinates, the potential energy surface is given by analytical approximations of terms of one, two, up to N particles of the form:

$$\mathcal{V}\left(\vec{r}\right) = \sum_{i=1}^{N} \mathcal{V}_1\left(\vec{r}_i\right) + \sum_{i<j}^{N} \mathcal{V}_2\left(\vec{r}_i, \vec{r}_j\right) + \sum_{i<j<k}^{N} \mathcal{V}_3\left(\vec{r}_i, \vec{r}_j, \vec{r}_k\right) + ... \tag{2.13}$$

Where $\vec{r} = \{\vec{r}_1, \vec{r}_2, ..., \vec{r}_N\}$ is the vector describing the positions of all particles in space.

An observable quantity in Molecular Dynamics simulations must first be expressed as a function of distance and momentum. This can be easily achieved from Hamilton's equations of motion:

$$\frac{\partial \vec{r}_i}{\partial t} = \vec{v}_i = \frac{\vec{p}_i}{m_i} \tag{2.14}$$

$$\frac{\partial \vec{p}_i}{\partial t} = -\frac{\partial \mathcal{V}\left(\vec{r}\right)}{\partial \vec{r}_i} = \vec{F}_i \tag{2.15}$$

hence
$$m_i \frac{\partial^2 \vec{r}_i}{\partial^2 t} = \vec{F}_i \tag{2.16}$$

where F_i is the force acting on atom i. This 2nd order differential equation is Newton's second law of motion. The force acting on an atom may be written as a function of the potential energy $V\left(\vec{r}\right)$:

$$\vec{F}_i = -\vec{\nabla}_{\vec{r}_i} \mathcal{V}\left(\vec{r}\right) \tag{2.17}$$

with the gradient applied by keeping all positions other than r_i constant. The Hamiltonian of the classical system can be calculated as

$$\mathcal{H}\left(\vec{r}, \vec{p}\right) = \sum_{i=1}^{N} \frac{\vec{p}_i^2}{2m_i} + \mathcal{V}\left(\vec{r}\right) \tag{2.18}$$

The most significant property of classical equations is the conservation law. This states that if the potential energy, $\mathcal{V}(\vec{r})$, and kinetic energy, $\mathcal{K}(\vec{p})$ do not depend explicitly on time, then the time derivative of the Hamiltonian is equal to zero.

$$\frac{d\mathcal{H}(\vec{r},\vec{p})}{dt} = \frac{d\left(\mathcal{K}(\vec{p}) + \mathcal{V}(\vec{r})\right)}{dt} = 0 \tag{2.19}$$

The conservation law is satisfied if there exist no explicitly time (or velocity) dependent forces acting on a system. A second important property is the time reversibility of the equations of motion. This means that changing the signs of the velocities will retrace their trajectories backwards.

Several algorithms have been proposed for the integration of the equations of motion. The most frequently used is the Verlet algorithm which is based on Taylor expansions of coordinates and velocities of an atom around time t.

$$\vec{r}(t+\Delta t) \approx 2\vec{r}(t) - \vec{r}(t-\Delta t) + \frac{\vec{F}(t)}{m}\Delta t^2$$
$$\vec{v}(t) = \frac{\vec{r}(t+\Delta t) - \vec{r}(t-\Delta t)}{2\Delta t} + O\left(\Delta t^2\right) \tag{2.20}$$

Other popular schemes of the so-called Verlet algorithms family are the Leap Frog, the velocity Verlet and the so-called Beeman[16] versions. Another family of algorithms utilizes higher-order methods, whose basic idea is to use information about positions and their first, second, and higher order time derivatives at time t in order to estimate the positions and their derivatives at time $t+\Delta t$.

Statistical mechanics provides the formalism for the macroscopic description of a system using information from its microscopic states. A statistical ensemble can be considered as a set of different points in phase space. Equilibrium Molecular Dynamics are conducted in the microcanonical (*NVE*) statistical ensemble. The macroscopic variables of the microcanonical ensemble are quantities that influence the nature of the system's internal states and more specifically: the total number of particles in the system (*N*), the system's volume (*V*), as well as the total energy in the system (*E*). In the case that the properties should be computed in constant pressure and temperature (*NPT* ensemble) modifications in Newton's equation of motion should be taken into account. To this end, thermostat and barostat terms are applied in the calculation of the total force acting on the particles.

In real systems the temperature is kept constant as it interacts with a heat reservoir, which has much larger heat capacity compared to the real system. In a microscopic description, the temperature is changing as a result of collisions between particles of the system and particles that are located close to the heat reservoir. The temperature of the system is related to the time average of the velocity of the particles via the following relation:

$$\left\langle \sum_i^N \frac{1}{2} m_i v_i^2 \right\rangle = \frac{3}{2} N k_B T \qquad (2.21)$$

where k_B is the Boltzmann constant and $\vec{v}_i$ is the velocity of a particle indexed as i.

Two types of algorithms were initially presented in the literature for temperature control: deterministic algorithms (Berendsen[17]) and stochastic algorithms (Andersen[15]). In the second case the dynamics of the system are disrupted due to the stochastic change in the velocities. The pressure calculation from a particle system is not as direct as the temperature. According to the Virial theorem in three dimensions, the pressure is computed through the relation

$$P = \frac{N k_B T}{V} + \frac{1}{3V} \sum_{i=1}^N \vec{r}_i \cdot \vec{F}_i \qquad (2.22)$$

Many of the methods used for the control of pressure are analogous to those used for constant temperature simulations. The volume may be changed by scaling the positions of the particles through a coupling parameter. Otherwise, the Nosé-Hoover[18] scheme can be applied using an external piston as additional degree of freedom.

In this study the simulations have been conducted in the *NPT* ensemble using the algorithm proposed by Martyna, Tobias and Klein.[19] This method is an extension of the method proposed by Parrinello and Rahman.[20] The temperature and pressure control is achieved by introducing thermostat and barostat terms that act as external forces to the equations of motion.

2.3. Force Field and Computational Details

2.3.1. Empirical Force fields

Two empirical force fields[7,21] have been used in this study for the quantification of atomic interactions. The first one is a compilation of well-known force field from the literature. The bonded interactions are taken from the Generalized Amber Force Field (GAFF)[22] and Optimized Potential for Liquids Simulations (OPLS)[23,24] force fields and are described by the equation 2.23.

$$E_{\text{bonded}} = \sum_{\text{bonds}} k_b \left(r - r_0 \right)^2 + \sum_{\text{angles}} k_a \left(\theta - \theta_0 \right)^2 +$$

$$+ \sum_{\text{dihedrals}} \sum_{n=1}^{3} \frac{V_n}{2} \left[1 + (-1)^n \cos(n\varphi) \right] + \sum_{\text{dihedrals}} \sum_{n=1}^{6} V_n \cos^n \varphi \qquad (2.23)$$

The last proper dihedral term is proposed by Marcon et al[25] in order to account the tendency of the side chains to arrange themselves in a perpendicular manner with respect to the polyaromatic cores. The non- bonded interactions, namely van der Waals and electrostatic interactions are quantified by Lennard Jones (6-12) and Coulomb potentials, respectively. The Lennard-Jones potential[23,24] is expressed as:

$$E_{\text{L-J},ij} = 4\varepsilon_{ij} \left[\left(\frac{\sigma_{ij}}{r_{ij}} \right)^{12} - \left(\frac{\sigma_{ij}}{r_{ij}} \right)^{6} \right] \qquad (2.24)$$

where the depth of the potential well ε_{ij} is a measure of how strongly atoms attract each other. In the case of unlike atoms ε_{ij} is calculated as the geometric mean:

$$\varepsilon_{ij} = \sqrt{\varepsilon_i \varepsilon_j} \qquad (2.25)$$

where ε_i and ε_j are the potential well-depths of atoms indexed as i and j.

The collision diameter σ_{ij} is the internuclear distance at which the intermolecular potential between atoms labelled as i and j is zero. For heteroatomic combinations the following mixing rule is adopted.

$$\sigma_{ij} = \frac{1}{2} \left(\sigma_i + \sigma_j \right) \qquad (2.26)$$

Eqs 2.25 and 2.26 together are known as the Lorentz-Berthelot combining rules. The Coulomb[7] potential quantifies the electrostatic interaction between atoms with partial charges q_i and q_j, separated by distance r_{ij}.

$$E_{\text{Coulomb},ij} = \frac{1}{4\pi\varepsilon\varepsilon_0} \frac{q_i q_j}{r_{ij}} \qquad (2.27)$$

The total potential of the empirical force field is defined as:

$$E_{\text{total}} = E_{\text{bonded}} + E_{\text{L-J}} + E_{\text{Coulomb}} \qquad (2.28)$$

The second utilized force field is the 2nd generation COMPASS force field[21]. The functional form of COMPASS is described by the following equation:

$$E_{\text{total}} = \sum_b \left[k_2 (b-b_0)^2 + k_3 (b-b_0)^3 + k_4 (b-b_0)^4 \right] +$$

$$\sum_\theta \left[k_2 (\theta-\theta_0)^2 + k_3 (\theta-\theta_0)^3 + k_4 (\theta-\theta_0)^4 \right] +$$

$$\sum_\varphi \left[k_1 (1-\cos\varphi) + k_2 (1-\cos 2\varphi) + k_3 (1-\cos 3\varphi) \right] +$$

$$\sum_\chi k_2 \chi^2 + \sum_{b,b'} k (b-b_0)(b'-b'_0) + \sum_{b,\theta} k (b-b_0)(\theta-\theta_0) + \quad (2.29)$$

$$\sum_{b,\varphi} (b-b_0) \left[k_1 \cos\varphi + k_2 \cos 2\varphi + k_3 \cos 3\varphi \right] +$$

$$\sum_{\theta,\varphi} (\theta-\theta_0) \left[k_1 \cos\varphi + k_2 \cos 2\varphi + k_3 \cos 3\varphi \right] + \sum_{\theta,\theta'} k (\theta'-\theta'_0)(\theta-\theta_0) +$$

$$\sum_{\theta,\theta',\varphi} k (\theta'-\theta'_0)(\theta-\theta_0)\cos\varphi + \frac{1}{4\pi\varepsilon_0} \sum_{i,j} \frac{q_1 q_2}{r_{ij}} + \sum_{i,j} \varepsilon_{ij} \left[2 \left(\frac{r_{ij}^0}{r_{ij}} \right)^9 - 3 \left(\frac{r_{ij}^0}{r_{ij}} \right)^6 \right]$$

The potential energy can be divided into two categories: valence terms including diagonal and off diagonal cross-coupling terms, and non-bonded interaction terms. The first four sums in the force field equation correspond to the diagonal valence terms and represent the energies required to deform internal coordinates (with values b, θ, φ, χ) from their reference values, denoted with subscript 0. These terms reflect the energy needed to stretch bonds (b), bend angles (θ) away from their reference values, rotate torsions (φ) by twisting atoms about the bond axis that determines the torsion angle, and distort atoms in planar bonded arrangements out of their equilibrium plane (χ). The next six terms are referred to as off-diagonal cross-coupling terms that include combinations of two or three internal coordinates.

The last two sums represent non-bonded interactions. In the case of like atoms, the parameters (ε, r) for the Lennard-Jones potential are given from the last term of the equation above. For unlike atoms a 6th power combining rule is used:

$$r_{ij}^0 = \left(\frac{\left(r_i^0\right)^6 + \left(r_j^0\right)^6}{2} \right)^{1/6} \quad (2.30)$$

$$\varepsilon_{ij} = 2\sqrt{\varepsilon_i \varepsilon_j} \left(\frac{\left(r_i^0\right)^3 \cdot \left(r_j^0\right)^3}{\left(r_i^0\right)^6 + \left(r_j^0\right)^6} \right) \quad (2.31)$$

As far as the electrostatic interactions are concerned, they are determined by using atomic partial charges. In the COMPASS force field, bond increments δ_{ij} represent the charge separation between atoms. The partial charge of an atom, labeled with index i, is equal to the sum of bond increments.

$$q_i = \sum_j \delta_{ij} \qquad (2.32)$$

where j represents all valence-bonded atoms to atom i.

2.3.2. Computational Details

All MM and MD calculations are carried out using the LAMMPS[26] package. The integration of equations of motion during MD simulations in the isothermal-isostress (NPT) ensemble is based on the Martyna-Tobias-Klein[19] algorithm using a time constant of 100fs for temperature and 2500fs for pressure control. In all MD simulations, a timestep of 1fs has been used and typical periodic boundary conditions have been applied in all dimensions. Long range interactions have been calculated in reciprocal space using the Particle-Particle-Particle-Mesh (PPPM) technique.[27] All systems are studied at room temperature (300K) and at elevated temperature of 400K via MD simulations. In special cases where high energy barriers hindered the evolution of studied phenomena, simulations at higher temperatures were employed. The quantification of particle interactions is accomplished through the empirical force field[7] (described in the previous section) capable of capturing the properties of such materials.

2.4. Results and Discussion

2.4.1 Molecular dimer and molecular wire calculations

Three different types of discotic PAHs have been examined: HBC, C96 and C132. In this study, a series of discotic dimers corresponding to various geometries has been examined via MM simulations.

Initially, single molecule geometries are constructed, with six n-hexane aliphatic side chains attached around the periphery of HBC and C96, whereas eight side chains are grafted to C132. The general procedure for dimer creation is outlined in the following steps: 1) for a given molecule (basis molecule), a second identical molecule is placed on top, at a constant distance of 3.4Å, in a manner that disk planes are parallel to each other and the vector that connects the centers of mass of PAHs is perpendicular to both planes. 2) Next, the PAH on top is rotated by a finite twist angle. 3) Lastly, the molecule on top is displaced to a variety of

distances (from 0Å to 4.2Å with a step of 0.7Å) and towards a multitude of directions parallel to the disk plane. The total number of stacking patterns that have been investigated is equal to 252 in the case of HBC, 1008 for C132 and 2268 for C132. Each system has been equilibrated using the Conjugate Gradient energy minimization scheme.[11,12] To increase the reliability of this study both empirical first generation[7] and second generation force fields are used. The minimizations have been carried out for a range of energy tolerances between 10^{-6} and 10^{-11} kcal/mol. Results of energy minimization are presented as energy states diagrams corresponding to minimized structures. Each horizontal line is a minimum energy configuration of the dimer. Horizontal lines which appear thicker actually represent several local energy minima that are almost on top of each other and minimum energy configurations are used for the determination of preferable stacking patterns. Energy minimizations have been employed utilizing the COMPASS force field. In the figures below the potential energy is presented as energy state diagrams.
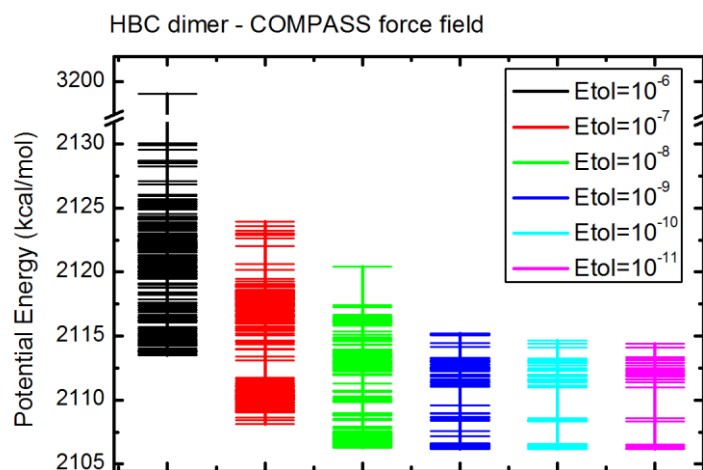
Figure 2: The potential energy of a HBC dimer utilizing the COMPASS force field.
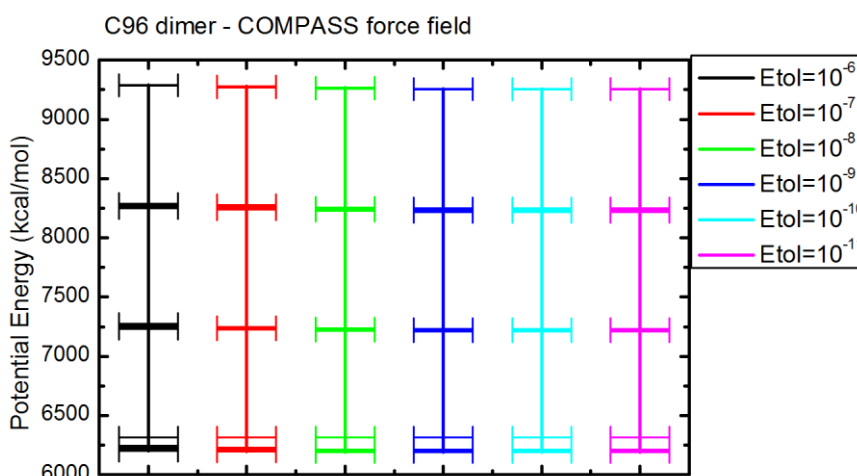
Figure 3: The potential energy of a C96 dimer utilizing the COMPASS force field.

13
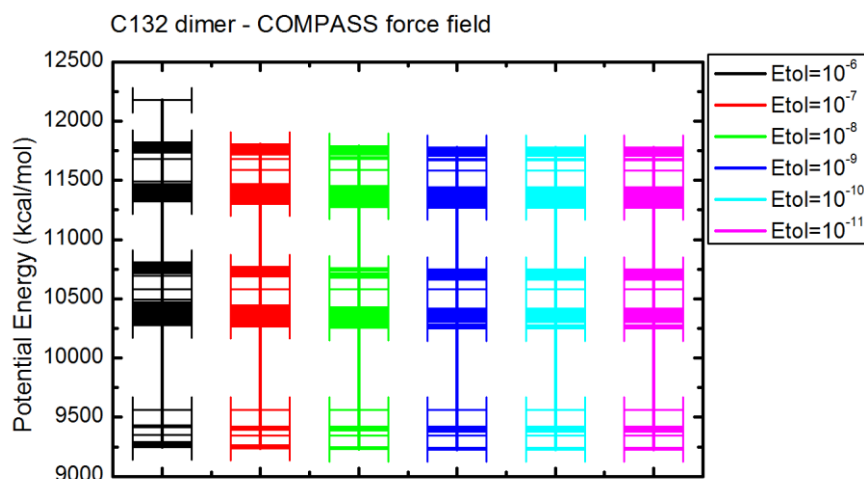
Figure 4: The potential energy of a C132 dimer utilizing the COMPASS force field.

To increase the reliability of this study, energy minimizations have been employed with CGenFF[28,29] and a hybrid all-atom/united-atom[7] force field published in the literature. The same lowest energy stacking patterns were obtained with all utilized force fields, and thus the simplest force field which is the hybrid one was used in simulations of molecular wires and crystals as it requires less computational resources.

As far as HBC-C6 is concerned, the lowest energy states correspond to two configurations: a parallel-displaced, graphitic-like motif, and a twisted by 30° stacking pattern. C96-C6 shows two preferable stacking patterns: a 20° twist angle stacking pattern and a graphitic-like AA stacking corresponding to a 60° twist angle. In the case of C132, three rotational profiles arise with twist angles of 20°, 60° (graphitic-like) and 90°, respectively. The aforementioned lowest energy dimer geometries are illustrated in figures 5-7. The lowest energy stacking patterns are used for the creation of initial configurations of molecular wires.
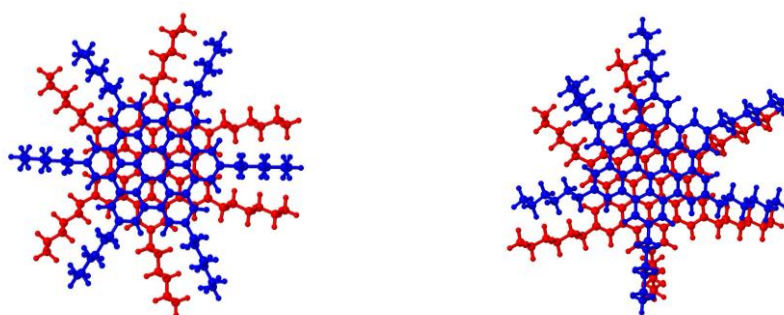
Figure 5: Lowest energy stacking patterns for HBC-C6 dimers: left) 30° stacking pattern, right) parallel-displaced graphitic like motif.

14
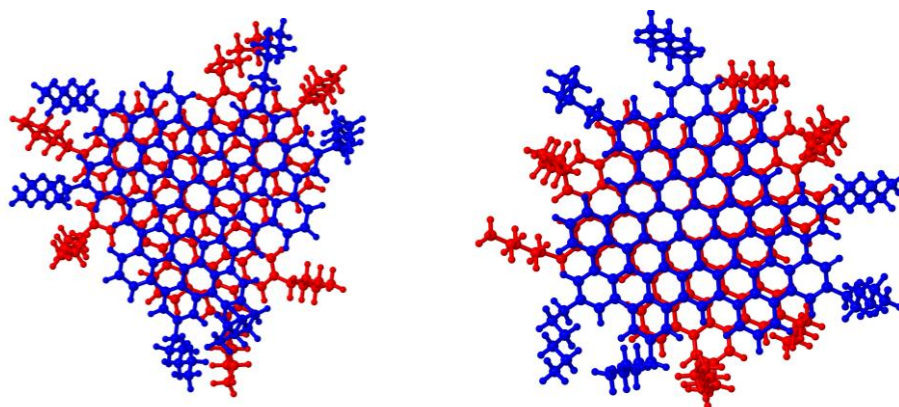
Figure 6: Lowest energy stacking patterns for C96-C6 dimers: left) 20° twist angle, right) graphitic-like 60° twist angle patterns.
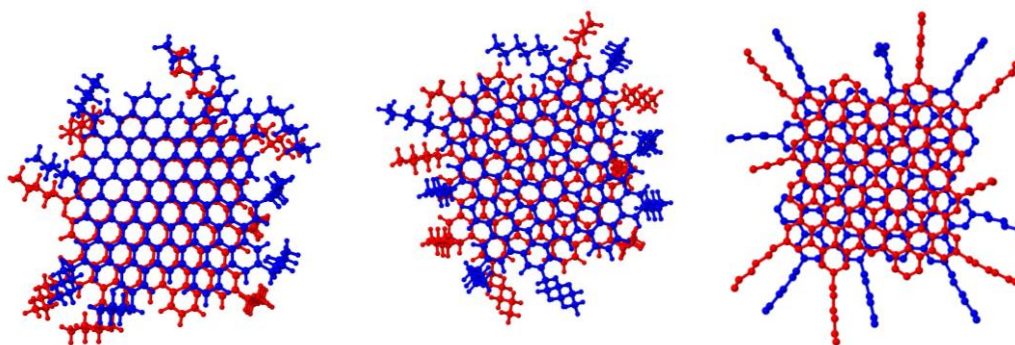
Figure 7: Lowest energy stacking patterns for C132-C6 dimers: left) graphitic-like 60° twist angle, middle) 20° twist angle and right) 90° twist angle patterns.

Relying on the stacking information gained from MM dimer calculations, a series of molecular wires are created. Wires comprised of C96 core molecules are constructed with 60 degrees twist angle and two variants based on the 20 degrees stacking motif: one helical and one alternating. In the case of C132, should symmetry be taken into account, five rotational profiles arise: three alternating with twist angle 20, 60 and 90 degrees and two helical at 20 and 60 degrees. Once the rotational state of the cores is established, a bond-by-bond Monte Carlo growth scheme[30] is utilized to create aliphatic side chains.

A simulation snapshot of a periodic wire consisting of twelve C96 molecules grafted with six C12 groups, which form an initial alternating profile of 60° twist angle (graphitic-like) is illustrated in the initial and final state after MD simulations at 300K and 400K. In all of the following figures, enlarged green spheres represent the linking carbon atoms of the polyaromatic cores where the side chains are grafted, blue atoms correspond to –CH$_2$- side chain units and red atoms to terminal –CH$_3$ units.
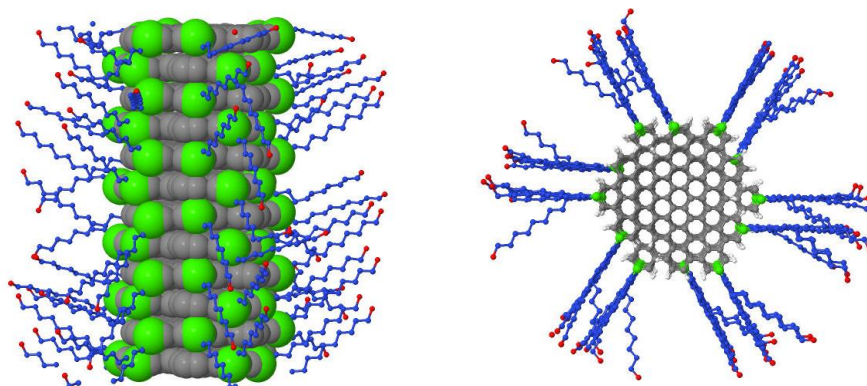
Figure 8: A C96-C12 molecular wire with a graphitic-like 60° twist angle profile at the initial simulation step at 300K: left) side view; right) top view.
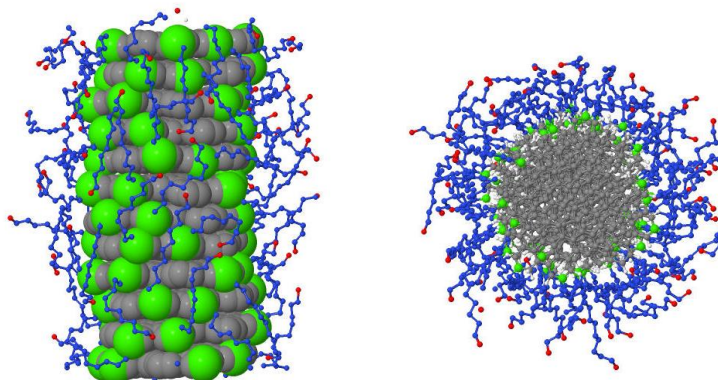
Figure 9: A C96-C12 molecular wire initially prepared with graphitic stacking after MD equilibration at 300K: left) side view; right) top view.
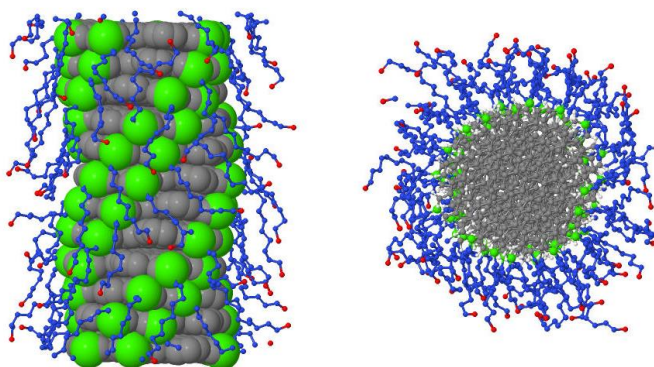
Figure 10: A C96-C12 molecular wire initially prepared with graphitic stacking after MD equilibration at 400K: left) side view; right) top view.

C132-phytyl molecular wires in their initial graphitic stacking and final form after MD simulations are illustrated in the following figures.
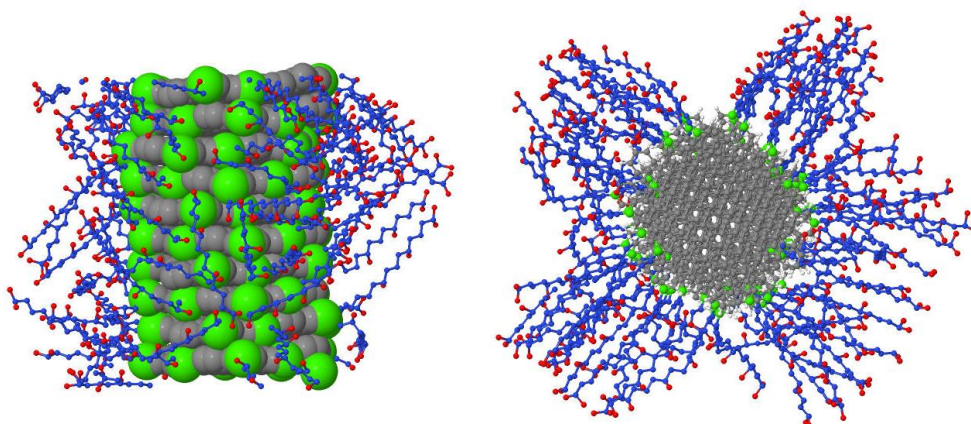
Figure 11 A C132-phytyl molecular in its initial state following a graphitic-like stacking pattern: left) side view; right) top view.
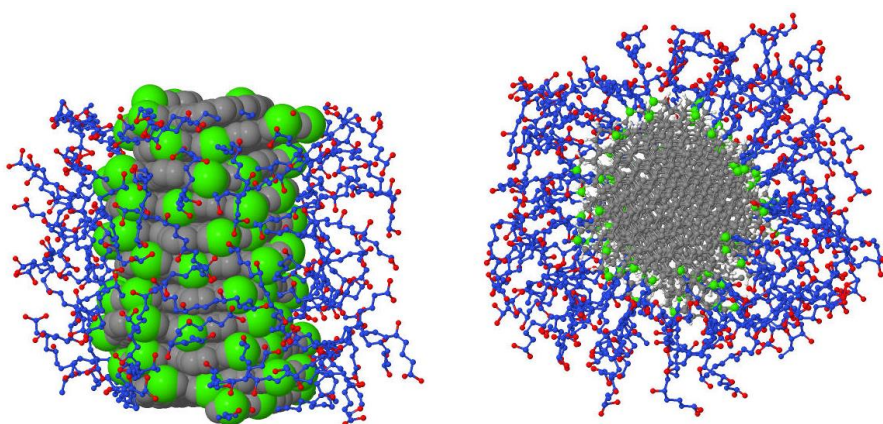
Figure 12: A C132-phytyl molecular wire with initial graphitic stacking after a MD simulation at 300K: left) side view; right) top view.
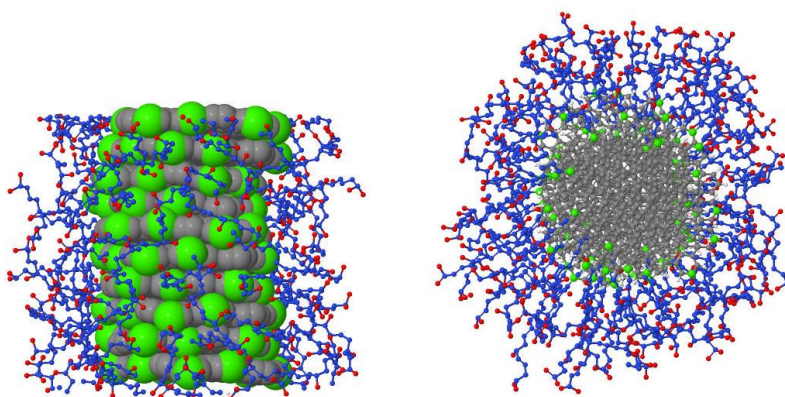
Figure 13: A C132-phytyl molecular wire with initial graphitic stacking after a MD simulation at 400K: left) side view; right) top view.

2.4.2. Cohesive energy of molecular wires

The cohesive energy of a single molecular wire is determined in two steps. First a system consisting of twelve discotic molecules is brought to equilibrium via MD simulation. Secondly, each discotic molecule is considered individually and its potential energy at every equilibrium snapshot is calculated. The cohesive energy can be determined by subtracting the sum of potential energies ($E_{mol,i}$) of each individual molecule from the potential energy of the wire (E_{wire}):

$$E_{coh} = E_{wire} - \sum_{i=1}^{N} \left(E_{mol,i} \right) \tag{2.33}$$

where N is the number of molecules. Each part of the right hand side of equation 2.33 can be decomposed into bonded and non-bonded terms:

$$E_{coh} = E_{wire}^{b} + E_{wire}^{nb} - \sum_{i=1}^{N} \left(E_{mol,i}^{b} + E_{mol,i}^{nb} \right) \tag{2.34}$$

The bonded interactions of the molecular wire are equal to the sum of bonded interactions of isolated disks. Also the non-bonded interactions are divided into intermolecular and intramolecular terms and cohesive energy reads:

$$E_{coh} = E_{wire}^{nb,inter} + E_{wire}^{nb,intra} - \sum_{i=1}^{N} \left(E_{mol,i}^{nb,inter} + E_{mol,i}^{nb,intra} \right) \tag{2.35}$$

Finally, the intramolecular energy of the whole wire is equal to the sum of intramolecular energies of individual disks and cohesive energy may be rewritten into:

$$E_{coh} = E_{wire}^{nb,inter} - \sum_{i=1}^{N} \left(E_{mol,i}^{nb,inter} \right) \tag{2.36}$$

Intermolecular energy values include reciprocal space energy components which are calculated using the PPPM technique.

As far as the systems under study are concerned, three different stacking patterns of C96-C12 molecules were examined, namely: a 20° helical pattern and a 60° and a 20° alternating pattern (the 60° could be also envisioned as a helical one since the 120° molecular symmetry of C96 supports this hypothesis). Cohesive energy results for the aforementioned systems are illustrated in the figures below.
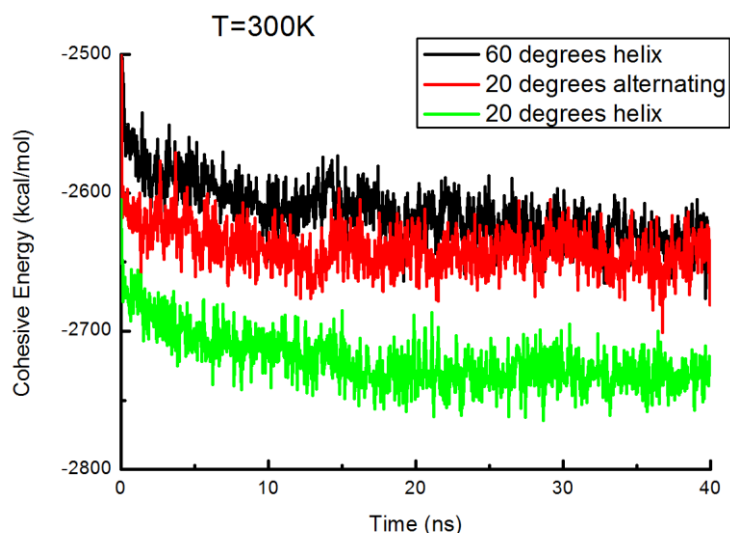
Figure 14: Cohesive energy of three C96-C12 systems at 300K.

At 300K it is evident that two cohesive energy profiles exist. The cohesive energy of C96-C12 60° helical system follows the same trend as the C96-C12 20° alternating system. In contrast, the 20° helical system has lower cohesive energy, which indicates a more stable structure.
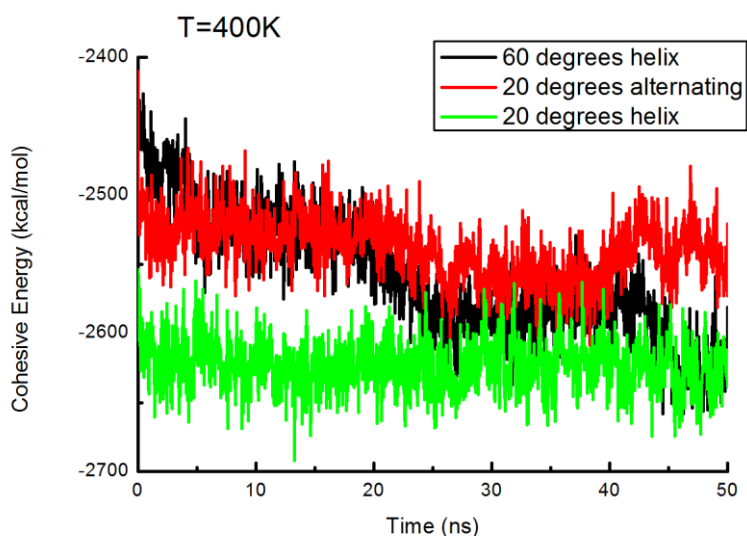
Figure 15: Cohesive energy of three C96-C12 systems at 400K.

At 400K two dominant profiles arise. The C96-C12 20° alternating system reaches a plateau at a higher energy level, while the other two systems reach a common plateau at approximately -2650 kcal/mol. At both temperatures, the 20° helix system is more stable. At 400K, the 60° helix tends to form a 20° helix while the 20° helix system does not change its structure. To quantify the helicity of the systems it was deemed necessary to calculate the

twist angle between neighboring aromatic molecules, alongside with other structural features listed in the following sections.

2.4.3. Twist angle

In this part, the twist angle of molecular pairs inside wires is evaluated. The twist angle is calculated by applying appropriate rotations about the normal to the core vector. We accept the smallest acute angle that brings the two molecular cores in perfect alignment. During this procedure, the information whether right or left hand rotation led to coincidence is stored in order to quantify the chirality of possible helical motifs. The twist angle between neighboring aromatic cores is calculated during MD simulations at 300K and 400K.
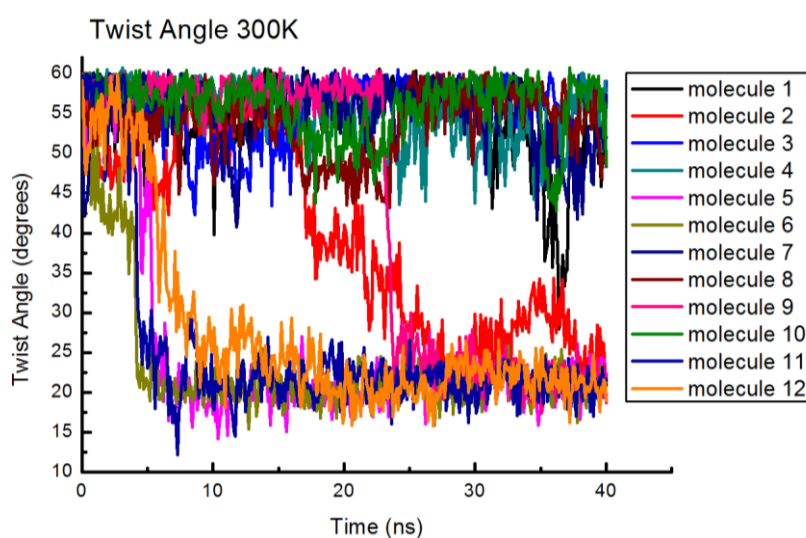
Figure 16: Twist angle time series of a wire consisting of twelve C96-C12 molecules with an initial graphitic stacking at 300K.

Twist angles seem to fluctuate around 60° for the first five nanoseconds of the simulation. As the system evolves in time, more neighboring molecules tend to form a 20° twist angle.
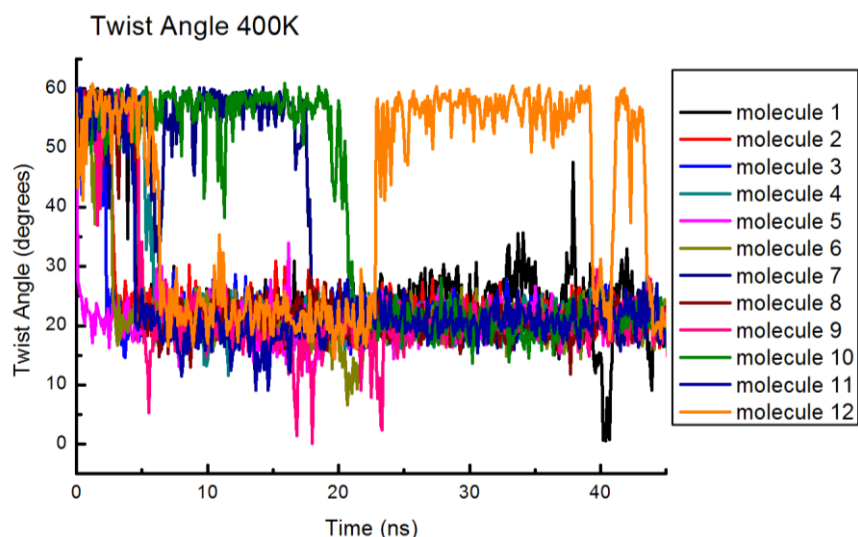
Figure 17: Twist angle time series of a wire consisting of twelve C96-C12 with an initial graphitic stacking at 400K.

In the case of 400K and after 40ns of simulation time, a 20° twist angle profile is dominant. In order to account for the possible helicity of the systems, we introduced the so called Chirality Index (CI) which is a measure that quantifies whether a right- or left- handed rotation can bring neighborhing polyaromatic cores into alignment. A CI of +1 corresponds to a right handed rotation, while -1 to a left handed rotation. In the figures below, CI of each molecular pair is plotted as a function of simulation time at 300K and 400K.
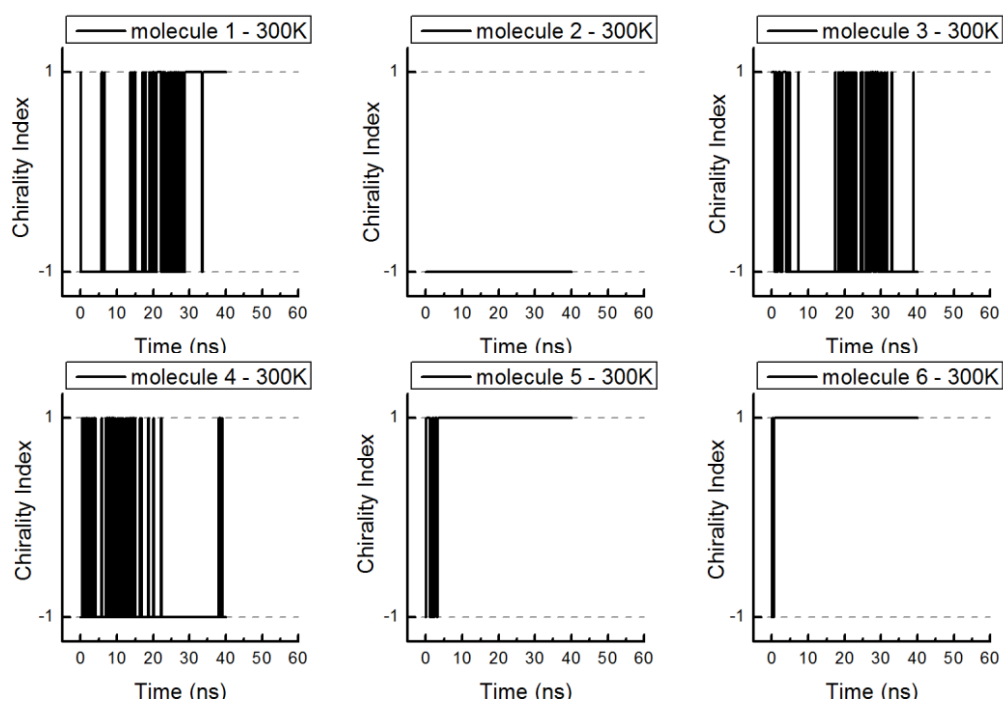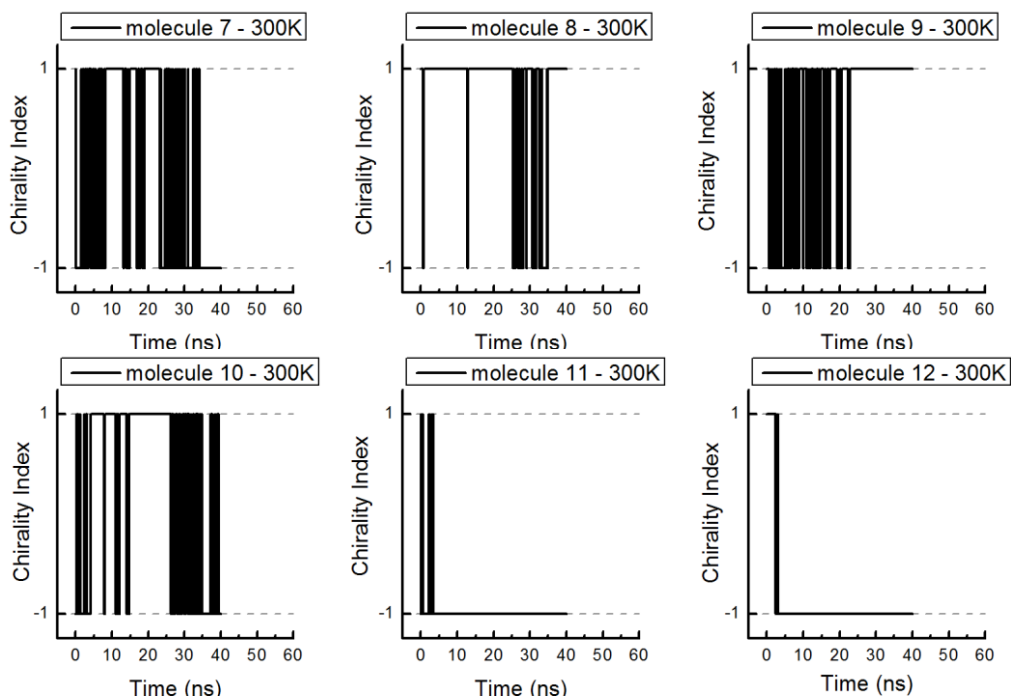
Figure 18: Chirality indices for a C96-C12 molecular wire initially prepared with a graphitic stacking at 300K.
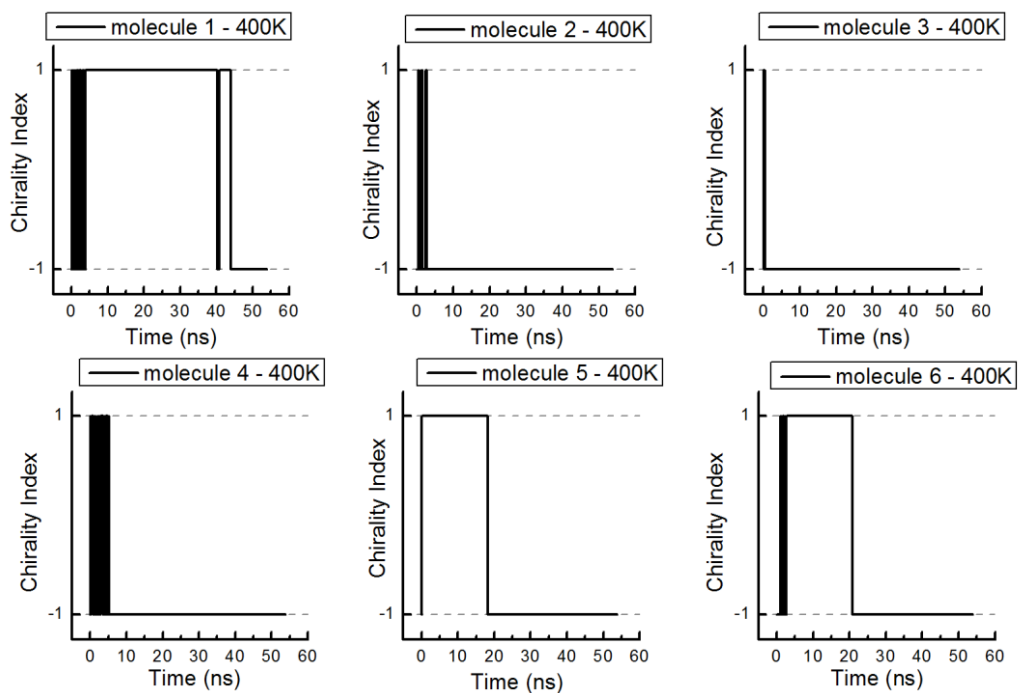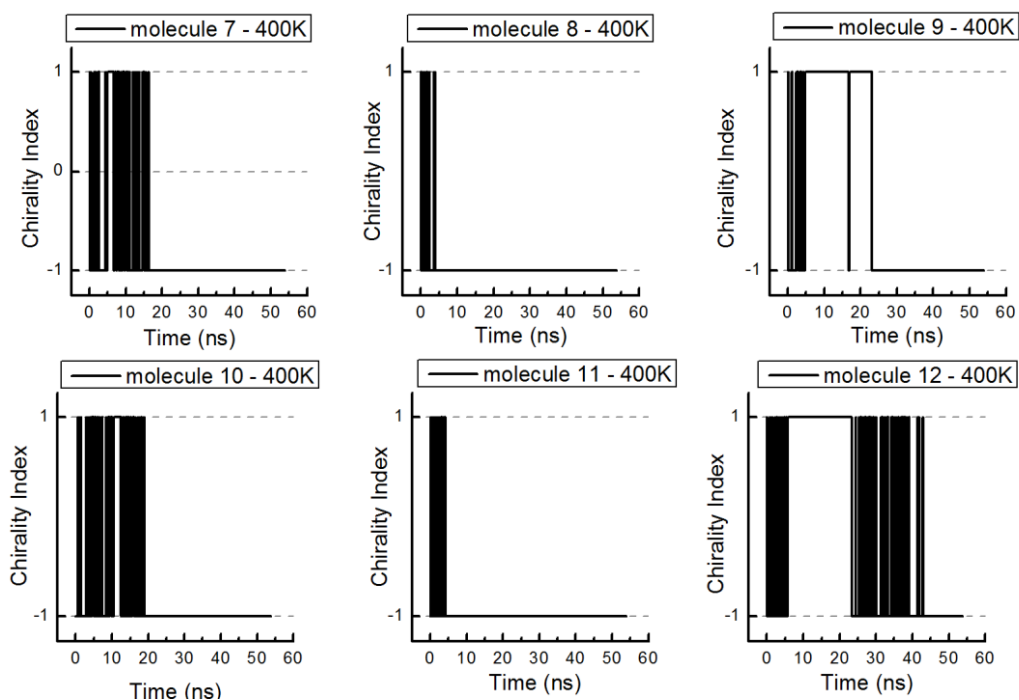
Figure 19: Chirality indices for a C96-C12 molecular wire initially prepared with a graphitic stacking at 400K.

At 300K, both right and left hand profiles exist. In contrast, at 400K, all molecules within the wire ultimately show a left handed helix. This indicates a perfect helical stacking within the molecular wire.

Furthermore, molecular wires comprised of C132 cores grafted with phytyl groups that form a 60° alternating and a 60° helical profiles, both graphitic-like, are examined. MD simulations have been carried out for a temperature range between 300K and 600K with a step of 100K. Higher temperatures were utilized in order to surpass energy barriers associated with the higher molecular weight of this system that leads to deceleration of system evolution. Twist angle time series diagrams are depicted in the following figures.

23
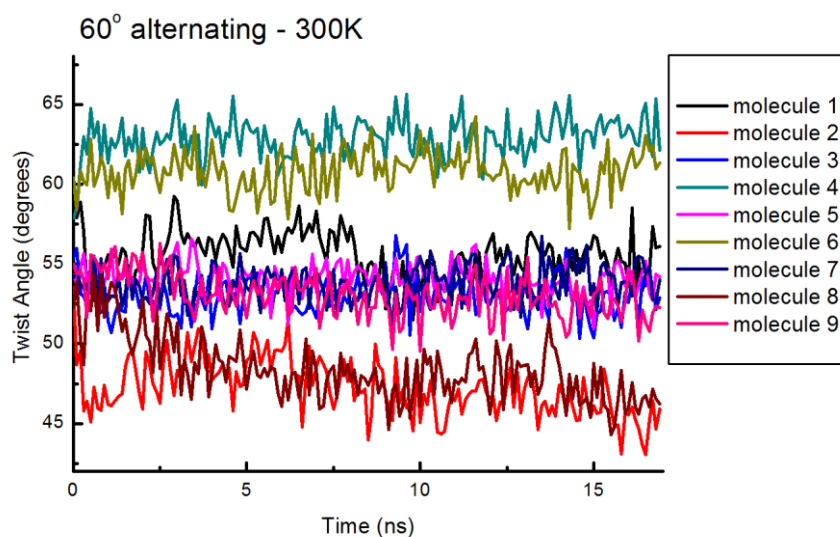
Figure 20: Twist angle time series of a C132-phytyl molecular wire with initial 60° graphitic-like alternating stacking pattern at 300K.
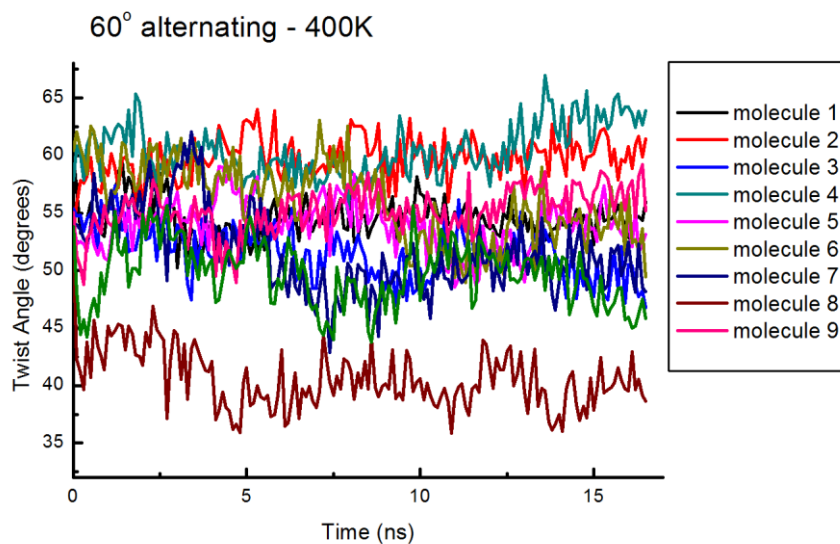
Figure 21: Twist angle time series of a C132-phytyl molecular wire with initial 60° graphitic-like alternating stacking pattern at 400K.
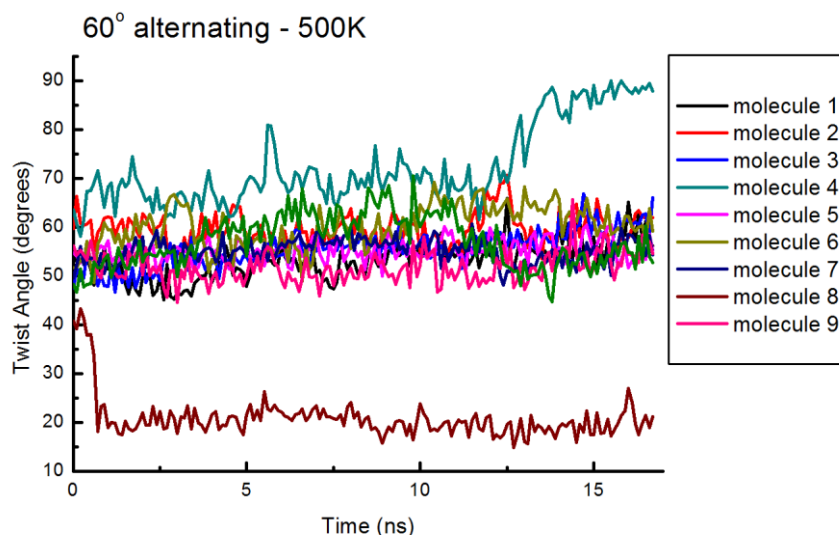
Figure 22: Twist angle time series of a C132-phytyl molecular wire with initial 60° graphitic-like alternating stacking pattern at 500K.
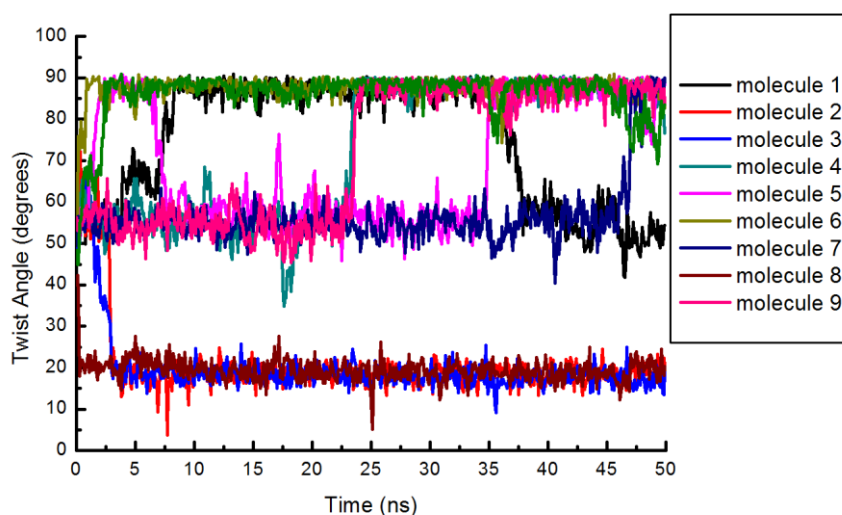
Figure 23: Twist angle time series of a C132-phytyl molecular wire with initial 60° graphitic-like alternating stacking pattern at 600K.

Initially at 300K, three families are identified at 62.5°, 52.5° and 47.0°. At the highest temperature (600K), two twist angle families are dominant, with the molecules forming 60° and 90° twist angle patterns.

As far as the C132-phytyl molecular wires with a 60° helical profile are concerned, results of our analysis are illustrated in the figures below.

25
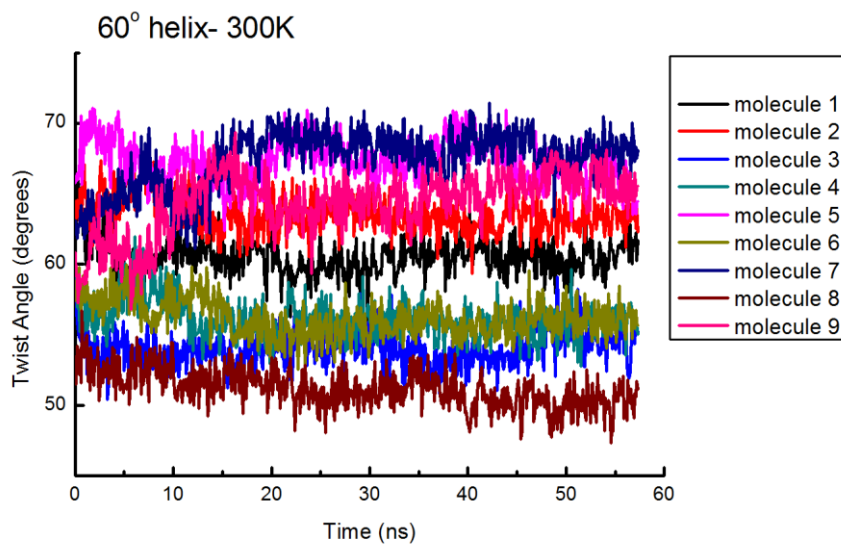
Figure 24: Twist angle time series of a C132-phytyl molecular wire with initial 60° graphitic-like helical stacking pattern at 300K.
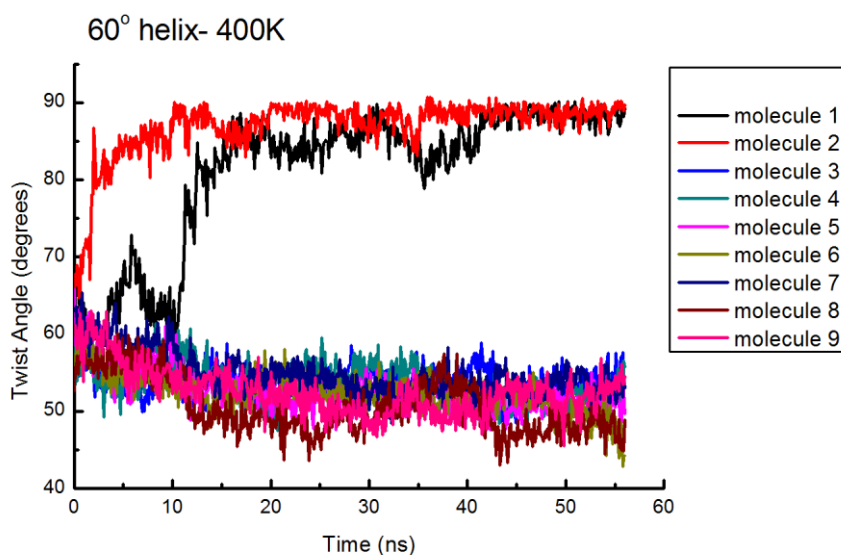
Figure 25: Twist angle time series of a C132-phytyl molecular wire with initial 60° graphitic-like helical stacking pattern at 400K.
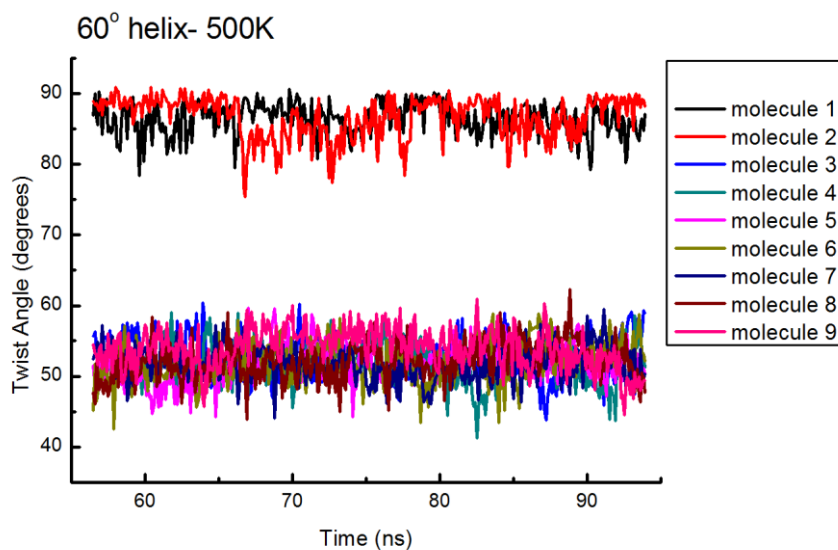
Figure 26: Twist angle time series of a C132-phytyl molecular wire with initial 60° graphitic-like helical stacking pattern at 500K.
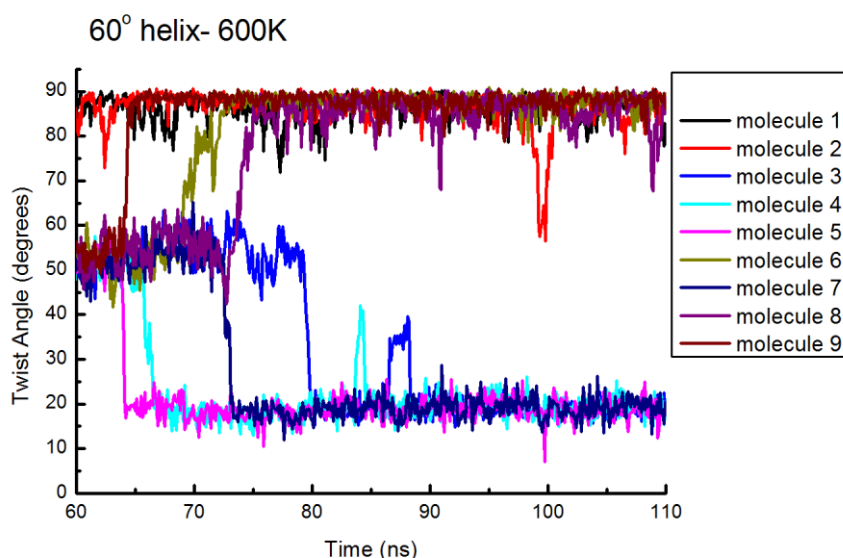
Figure 27: Twist angle time series of a C132-phytyl molecular wire with initial 60° graphitic-like helical stacking pattern at 600K.

At 300K, twist angle time series fluctuate around 50° and 70°. At 600K, twist angles tend to reach plateaus at 20° and 90°.

2.4.4. Axial distance & disk tilt

The axial direction vector $\vec{n}$ is calculated by means of Orthogonal Distance Regression (ODR) calculations taking into consideration the center of mass of each disk. The normal distance between the carrier of vector $\vec{n}$ and the center of mass of each disk is referred to as the axial distance. Also the tilt of each molecule is calculated from the angle formed between the axial distance vector and the vector $\vec{p}$ that is perpendicular to the disk plane. In the

27

figures below the axial distance and the tilt angle of the discotics under study are plotted as a function of simulation time.
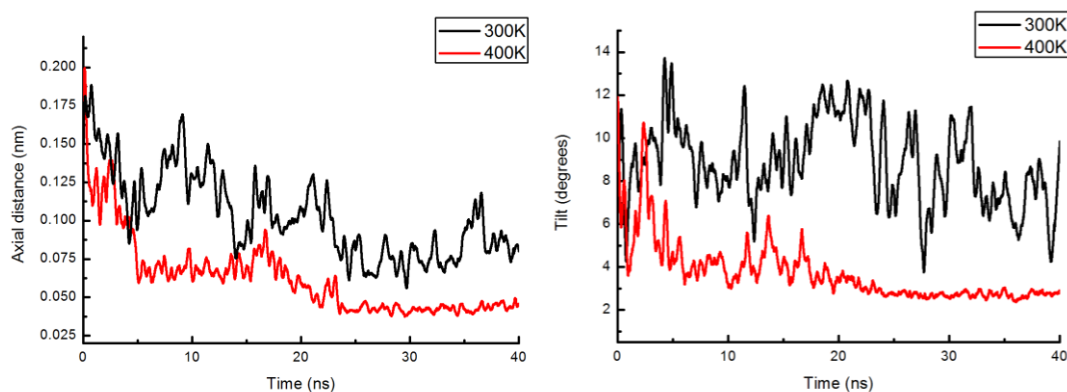
Figure 28: Left) Axial distance for C96-C12 initially prepared with a graphitic-like stacking pattern at 300K and 400K. Right) Tilt of the same system at 300K and 400K.

As temperature increases, both axial distance and tilt drop. The axial distance fluctuates around 0.10 and 0.05 nm at 300K and 400K, respectively. At 300K the tilt fluctuates rapidly around 6° and 14°. At 400K the tilt angle reaches a plateau of ~4° and the molecules are well aligned within the molecular wire and with respect to the axial direction.
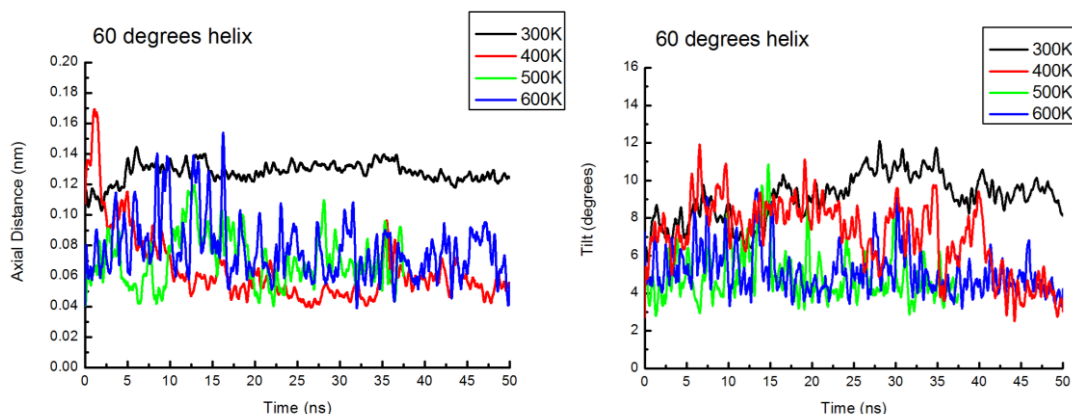
Figure 29: Axial distance of the 60 degrees alternating C132-phytyl system at a temperature range between 300K and 600K with a step of 100K.

At 300K both axial distance and tilt follow a higher trend. As temperature increases, axial distance and tilt reach a plateau 0.06nm and 4°, respectively.
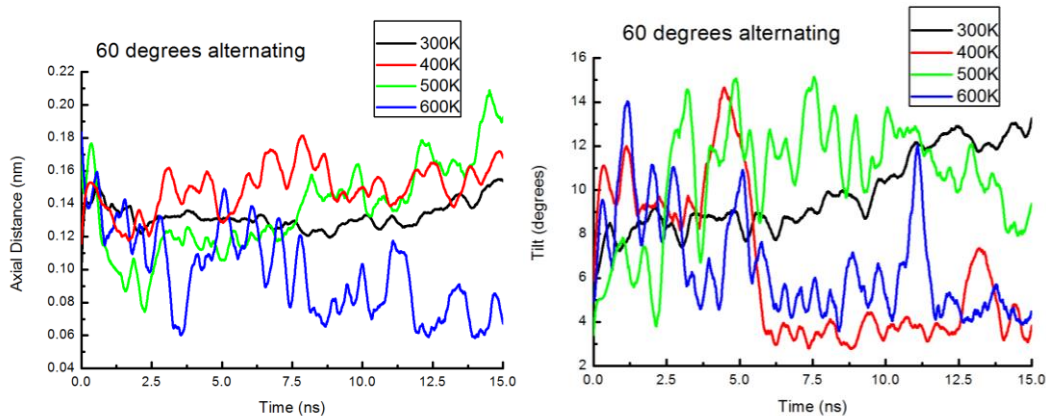
Figure 30: Axial distance of the 60 degrees helical C132-phytyl system at a temperature range between 300K and 600K with a step of 100K.

The behavior of the axial distance and tilt in the case of C132-phytyl with a 60° helix system cannot be described sufficiently, as more simulation time is required. Regardless, the temperature rise leads to a decrease of the aforementioned structural parameters.

2.4.5. Dynamical properties

In this section, a quantification of the molecular motion of the side chains is attempted via dynamical studies. The dynamical property calculated is related to the time correlation of the side chain end to end vector. This is the vector between a linking aromatic carbon atom and the terminal atom of the attached side chain. This quantification is carried out using the 2nd order Legendre polynomial autocorrelation function through the equation

$$P_2(\theta) = \frac{3}{2}\left\langle \cos^2 \theta(t) \right\rangle - \frac{1}{2}$$

(2.37)

where θ is the angle between a vector at time t=0 and the same vector at time t. The autocorrelation function of the P_2 polynomial of end-to-end vector is a measure of side chain mobility.
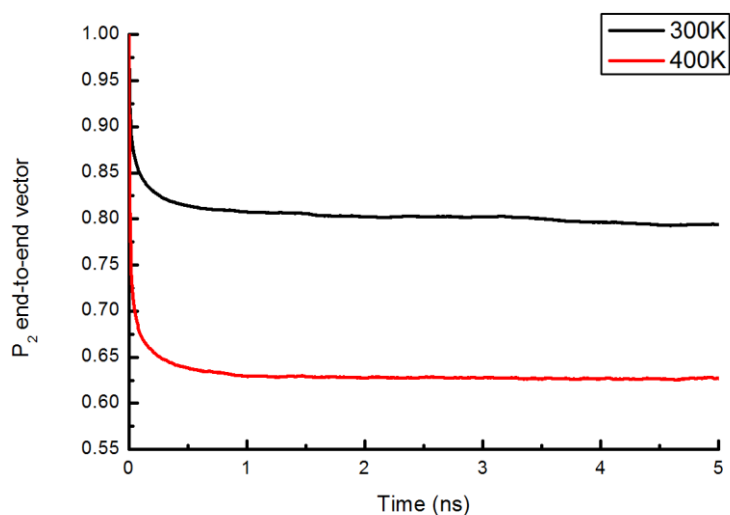
Figure 31: 2nd order Legendre polynomial autocorrelation function of the end-to-end side chain vector at 300K and 400K for the C96-C12 molecular wire initially created with a graphitic-like stacking pattern.

The end-to-end vector shows slower dynamics at 300K compared to 400K.
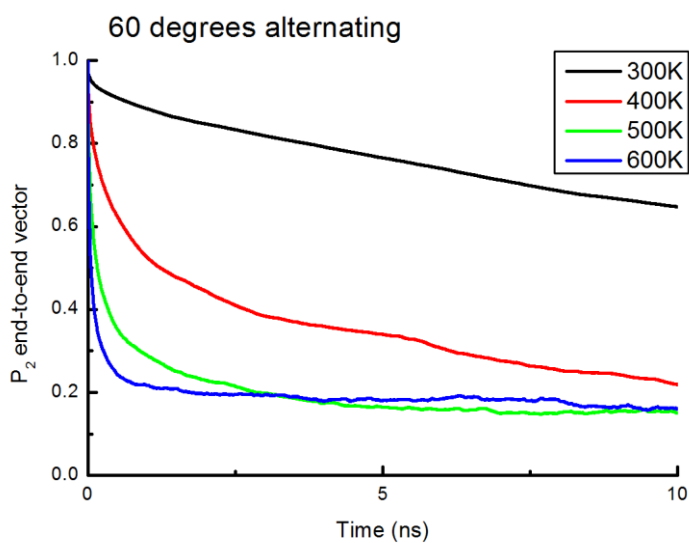
Figure 32: 2nd order Legendre polynomial autocorrelation function of the end-to-end side chain vector at various temperatures for the C132-phytyl molecular wire initially created with a graphitic-like stacking pattern with an alternating 60° twist angle.
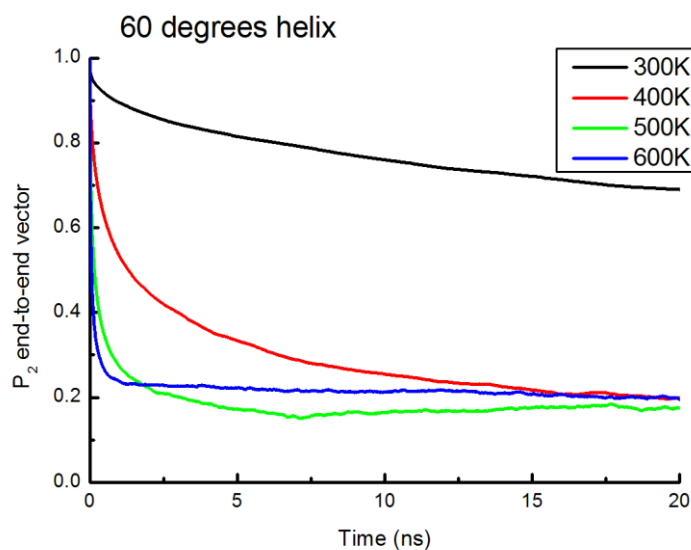
Figure 33: 2ⁿᵈ order Legendre polynomial autocorrelation function of the end-to-end side chain vector at various temperatures for the C132-phytyl molecular wire initially created with a graphitic-like stacking pattern with a helical 60° twist angle.

The dynamics of the end-to-end vector are faster as temperature increases for both C132-phytyl systems. It should be noted that C96-C12 molecular wires show abrupt plateaus in side chain dynamics, a behavior linked to neatly packed C12 side chains on the molecular wire core. The bulkier phytyl groups with protruding methyl units do not show this behavior due to their divergence from perfect linearity that the methyl groups create.

2.4.6. Generation of molecular crystals

Taking into account the results of the wires studies, a series molecular crystals comprised of aligned molecular wires have been constructed and equilibrated via MD simulations. These systems are the source data for XRD structural analyses described in the following chapter. A characteristic molecular crystal is illustrated in the following pictures.
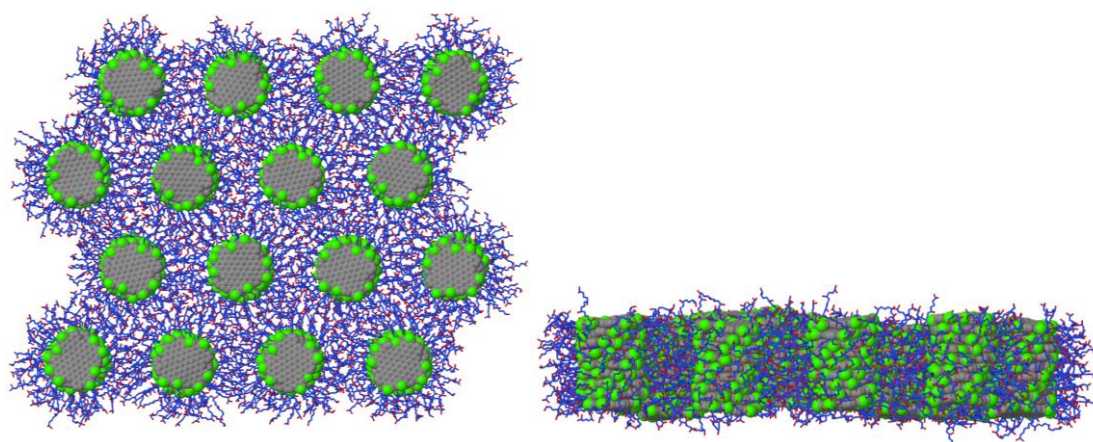
Figure 34: Top (left) and side (right) views of a C132-phytyl molecular crystal.

Chapter 3: X-Ray Diffraction and 2D Wide Angle X-Ray Diffraction

The main use of X-rays is for the determination of atomic structure of materials utilizing the principles of diffraction. The layout of this chapter is as follows. First we consider scattering from a free electron, secondly from two electrons, then scattering from an atom and a molecule, finally arriving at the description of diffraction from a bulk material. Special attention is given to benchmarking the methodology by analyzing diffractograms of prototype crystal structures. Finally, theoretical patterns from equilibrium MD trajectories are calculated and compared with experimental diffractograms.

3.1. Theoretical background[31–33]

3.1.1. Scattering from a free electron – Thomson effect

The particles in diffraction techniques have dual properties and behave as matter waves through the de Broglie relationship, $\lambda = h / p$, where λ is the wavelength, h is the Planck's constant (6.63×10^{-34} Js) and p is the magnitude of momentum. The propagation of a wave is described by the advancement of a wave front. Assuming a plane wave propagation, the wavevector $\vec{k}$ is perpendicular to the plane wave front. The relationship between $\vec{p}$ and $\vec{k}$ is:

$$\vec{p} = \frac{h}{2\pi} \vec{k} \tag{3.1}$$

From the de Broglie relationship one obtains $\left| \vec{k} \right| = \dfrac{2\pi}{\lambda}$. Note that the wavevector $\vec{k}$ has units of inverse length. Let $\vec{k}$ and $\vec{k}'$ denote the wavevectors of the incident (ingoing) and scattered (outgoing) waves, respectively. The difference in directions $\vec{k}$ and $\vec{k}'$ is referred as scattering angle *2θ* and the scattering vector or the wavevector transfer is defined as:

$$\vec{Q} = \vec{k} - \vec{k}' \tag{3.2}$$

Figure 35: The scattering triangle. $\vec{k}$ and $\vec{k}'$ represent the incident and scattered wavevectors, respectively. The angle between these wavevectors is 2θ.

Should elastic scattering be taken into consideration, when a free or weakly bound electron interacts with an X-ray beam, it is forced to oscillate with the same frequency. Consequently, the charged oscillating electron becomes a source of secondary radiation. The scattered wave has equal frequency with respect to the incident one, but lower amplitude. Thomson was the first who examined elastic scattering from electrons and thus this phenomenon is known as the Thomson effect. According to this assumption, the wavelength magnitude of ingoing and outgoing waves is the same, so that $\left|\vec{k}\right| = \left|\vec{k}'\right| = 2\pi / \lambda$. Furthermore, a hypothetical scattering triangle (Illustrated in the figure above) formed from the incident, scattered and scattering vectors is isosceles and the magnitude of the scattering wavevector is given by the following relation:

$$\left|\vec{Q}\right| = 2\left|\vec{k}\right|\sin\theta = \frac{4\pi}{\lambda}\sin\theta \tag{3.3}$$

3.1.2. Scattering from two electrons: Bragg condition

To begin with, let us consider scattering from two electrons separated by distance r. The position of the first electron coincides with the origin and the position of the second is defined by a vector $\vec{r}$. The wave scattered by the electron at position r has to travel a longer path than the one scattered at the origin. The phase retardation of the incident wave can be calculated as the scalar product between $\vec{k}$ and $\vec{r}$ ($\varphi_{in} = \vec{k} \cdot \vec{r}$). In the so called Fraunhofer limit, the phase difference between the scattered waves is $\varphi_{out} = \vec{k}' \cdot \vec{r}$. For two electrons separated by distance r, this difference can be calculated as the resulting phase difference ($\Delta\varphi$) between the scattered waves:

$$\Delta\varphi = \varphi_{in} - \varphi_{out} = \left(\vec{k} - \vec{k}'\right) \cdot \vec{r} = \vec{Q} \cdot \vec{r} \tag{3.4}$$
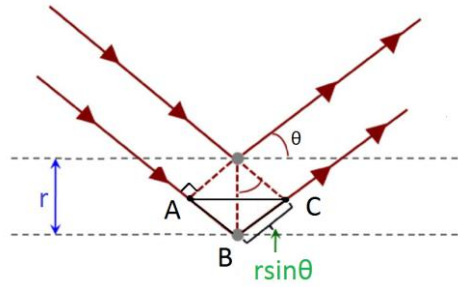
Figure 36: Scattering from two electrons separated by distance *r*.

To calculate the extra path of the wave scattered at position *r*, we define the triangle ABC from the points A, B and C, as illustrated in Figure 3.5. Point B coincides with the electron at position *r* and points A and C are the intercepts of normal directions with respect to the ingoing and outgoing waves. In the case where an electron is located at position *r*, the photons must travel a longer path which is equal to AB+BC. The triangle ABC is also isosceles and from trigonometry it can be shown that:

$$AB + BC = 2AB = 2r\sin\theta \tag{3.5}$$

For constructive interference to occur, both waves must scatter in phase. This means that the extra path is proportional to the wavelength.

$$2r\sin\theta = n\lambda, \qquad n = 1, 2, 3... \tag{3.6}$$

where *n* is an integer that represents the order of the reflection. This equation is known as Bragg's law and it is one of the most fundamental equations in crystallography.

3.1.3. Scattering from an atom: atomic form factor

We now turn to the problem of considering scattering from an atom consisted of *Z* electrons. In the classical, non-quantum, level of theory, atomic electrons may be viewed as a charge cloud surrounding the nucleus. According to the Lorentz oscillator model the interaction between atoms and electric field can be described by assuming that electrons are bound to atomic nucleus by a spring-like force, which is quantified by Hooke's Law. An applied electric field would displace charged electron leading into oscillating motion. As explained in 3.1.1. the accelerated electron emits secondary radiation. In this way the atom can be treated as an assembly of damped oscillators.

The electronic density number $\rho(\vec{r})$ is a function describing the charge distribution within the atom. The scattered radiation field is a superposition of contributions from different volume elements of this distribution. A volume element d^3r at position $\vec{r}$ will contribute an

amount of $\rho(\vec{r})d^3r$ to the total scattered field. The phase factor of the scattered field is defined as $e^{i\vec{Q}\cdot\vec{r}}$. This allows us to introduce the atomic form factor f^0:

$$f^0\left(\vec{Q}\right) = \int \rho(\vec{r})e^{i\vec{Q}\cdot\vec{r}}d^3r \qquad (3.7)$$

This term is also referred as the Thomson or non-resonant term because resonant effects have been neglected. In the limit where $\vec{Q}\to 0$, all atomic electrons scatter in phase and the form factor reaches its maximum value, which is equal to the atomic number Z. As $\vec{Q}$ increases, more atomic electrons start to scatter out of phase and f^0 drops. Consequently, the lowest value asymptotically decays to zero and it corresponds to $\vec{Q}\to\infty$. An alternative interpretation of these scattering limits is that when the wavelength of the incident radiation gets much smaller, compared to the electron size, then destructive interference occurs and the diffracted radiation tends to zero.

So far we have assumed that electrons respond to X-rays as if they were free. Atomic electrons are not free; they are bound to discrete energy states governed by the laws of quantum mechanics. The most tightly bound electrons are those closest to the nucleus, in the so-called K-shell. Electrons in upper shells (L, M, N..) are less tightly bound and will respond to the driving field of the incident radiation more promptly. Electrons can be treated as if they were free only at energies (or equivalently frequencies) much larger than the binding energy. Overall, it is expected that the radiation field will be reduced by some amount which is referred to as dispersion correction. This correction term is a complex number consisting of a real and an imaginary part commonly denoted as f' and f'', respectively. The real component displays resonant behavior at energies corresponding to atomic absorption edges. The imaginary part arises from energy dissipation mechanisms. Finally, it is worth mentioning that the non-resonant term has strong dependence on the wavevector transfer, while the dispersion terms are dominated by the X-rays frequencys $\hbar\omega$. To this end, the atomic form factor may be written as:

$$f\left(\vec{Q},\hbar\omega\right) = f^0\left(\vec{Q}\right) + f'\left(\hbar\omega\right) + if''\left(\hbar\omega\right) \qquad (3.8)$$

3.2. Kinematic Diffraction from Non-Crystalline Materials[31–33]

3.2.1. Scattering from a molecule

Having introduced scattering from a single atom, we are able to gradually expand our scope towards scattering from a molecule. The structure factor arising from a molecule can be derived by summing over the atomic form factors.

$$F^{mol}\left(\vec{Q}\right) = \sum_{j}^{N} f_j(\vec{Q}) e^{i\vec{Q}\cdot\vec{r}_j} \tag{3.9}$$

where index j indicates different atoms in a molecule consisted of N atoms and $\vec{r}_j$ is the position vector given by the equation:

$$\vec{r}_j = x_j \hat{x} + y_j \hat{y} + z_j \hat{z} \tag{3.10}$$

where x_j, y_j and z_j are the coordinates of the atom indexed as j. Equivalently, using fractional coordinates $x_j^{'}$, $y_j^{'}$ and $z_j^{'}$ defined as:

$$x_j^{'} = \frac{x_j}{L_x}, y_j^{'} = \frac{y_j}{L_y}, z_j^{'} = \frac{z_j}{L_x} \tag{3.11}$$

the position vector can be rewritten as:

$$\vec{r}_j = x_j^{'} \vec{a} + y_j^{'} \vec{b} + z_j^{'} \vec{c} \tag{3.12}$$

The exponential terms in the sum in equation 3.13 are of order unity since:

$$e^{i\vec{Q}\cdot\vec{r}_j} = \cos\left(\vec{Q}\cdot\vec{r}_j\right) + i\sin\left(\vec{Q}\cdot\vec{r}_j\right) \tag{3.13}$$

Consequently, the sum of the form factors is of order unity except when constructive interference occurs. As mentioned earlier, the condition for constructive interference is that the phase difference must be an integer multiple of the phase factor.

$$\vec{Q}\cdot\vec{r}_j = 2\pi \times n \tag{3.14}$$

where n is an integer. An elegant solution may be given by continuing the mathematical formulation in the reciprocal space via the equations:

$$\vec{a}^* = 2\pi \frac{\vec{b}\times\vec{c}}{\vec{a}\cdot(\vec{b}\times\vec{c})}, \ \vec{b}^* = 2\pi \frac{\vec{c}\times\vec{a}}{\vec{a}\cdot(\vec{b}\times\vec{c})}, \ \vec{c}^* = 2\pi \frac{\vec{a}\times\vec{b}}{\vec{a}\cdot(\vec{b}\times\vec{c})} \tag{3.15}$$

The position vector of the reciprocal lattice can be expressed as

$$\vec{s}^*_{hkl} = h\vec{a}^* + k\vec{b}^* + l\vec{c}^*$$ (3.16)

where h, k and l are the so called Miller indices. In this way the scalar product becomes:

$$\vec{r}_j \cdot \vec{s}^*_{hkl} = 2\pi(hx'_j + ky'_j + lz'_j)$$ (3.17)

The condition for constructive interference is satisfied only when the sum of the variables inside the parenthesis is equal to an integer number. This is similar to the Laue condition for diffraction, which states that if the wavetransfer vector $\vec{Q}$ coincides with the reciprocal lattice vector, the scalar product of the phase factor becomes non-vanishing and diffraction is realized.

3.2.2. Fiber Diffraction

A schematic representation of a fiber diffraction experimental setup is illustrated in the figure below[10]. By convention, the vertical fiber axis of the sample coincides with the c-axis, while the azimuthal orientation of the a-b plane is random[31] In a fiber diffraction[31] experiment the incident beam, with a wavevector $\vec{k}$, is perpendicular to the fiber axis. Bragg reflections occur on the equatorial (horizontal) plane according to the fact that the fiber sample consists of a bundle of filaments and provide information about the intercolumnar organization[10]. The periodicity of the filaments, along the c-axis, is giving rise to Bragg reflections on the meridional (vertical) plane, revealing the presence of intracolumnar order.
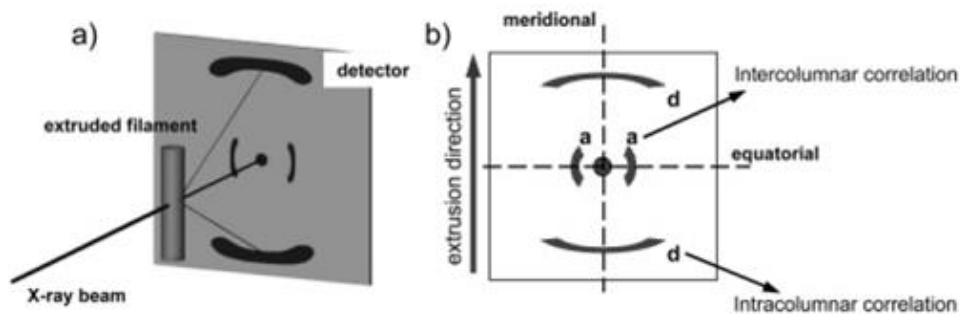
Figure 37: a) A schematic representation of a fiber diffraction experimental setup. The incident X-ray beam is perpendicular to the sample bearing cylindrical symmetry. b) A 2D WAXD pattern arising from a single filament. The intercolumnar distance in the equator and intracolumnar distance in the meridian are denoted as a and d, respectively.[10]

To evaluate intensity arising from a fiber sample it is convenient to decompose the reciprocal position vector into the vertical ($\vec{s}_z$) component and horizontal component ($\vec{s}_{xy}$). This can be easily done by transforming the vector $\vec{s}_{hkl}$ into cylindrical coordinates (r, φ, z) through the equations:

$$r = s_{xy}^* = \sqrt{\left(s_x^*\right)^2 + \left(s_y^*\right)^2} \tag{3.18}$$

$$s_z^* = s_z^* \tag{3.19}$$

$$\theta = \tan^{-1}\left(\frac{s_y^*}{s_x^*}\right) \tag{3.20}$$

where $r \in \{0, \infty\}, \theta \in \{0, 2\pi\}, z \in \{-\infty, \infty\}$. In terms of real space coordinates (x, y, z), the position vector in the reciprocal space is expressed as:

$$\begin{aligned} s_x^* &= r\cos\theta \\ s_y^* &= r\sin\theta \\ s_z^* &= s_z^* \end{aligned} \tag{3.21}$$

3.2.3. Approximations

Before we proceed to our analysis, it was deemed necessary to state all the approximations that took place.

1) In this study, it is assumed that scattering is elastic and the incident X-rays are monochromatic and coherent.

2) Secondly, the scattering is considered to be weak. This approach neglects multiple scattering effects and is also known as the kinematical approximation. In perfect crystals this approximation breaks down and dynamical diffraction occurs.

3) Furthermore, it is assumed that the source and detector are sufficiently far so that incident and scattered beams can be treated as plane waves. This is the so-called far-field limit (Fraunhofer diffraction).

4) The effect of thermal motion has been taken into account by calculating X-ray spectra as time averages from successive simulation snapshots. Therefore it was not necessary to resort to Debye thermal corrections.

3.3. Previous Work

A plethora of experimental studies for the determination of the structure of discotic PAHs by analyzing XRD and WAXD patterns can be found in the literature. An exhaustive experimental investigation for the three nanographene discotic molecules (HBC, C96 and C132) grafted with a variety of aliphatic chains have been conducted in the work Pisula et al[10] and Simpson et al[34]. A characteristic experimental WAXD diffractogram from a superphenalene molecule substituted with six n-dodecane aliphatic chains[9,10,35] is illustrated in the figure below:
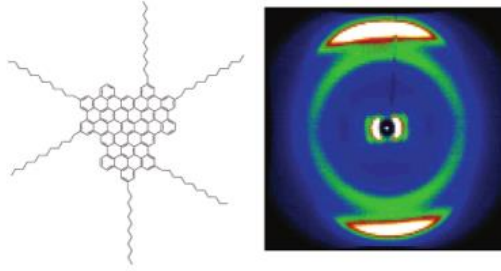
Figure 38: 2D-WAXD of a C96-C12 molecular crystal[10].

As far as computational studies are concerned, in the work of Breiby et al[36,37] and Marcon et al[25] WAXD patterns from perylene derivatives have been computed from MD trajectories. Furthermore, a combined computational and experimental study of propylene-butylene[38,39] copolymers and PBTTT-C$_{14}$ films[40] upon uniaxial stretching has been employed by Mao et al. [38,39,41]

3.4. Proposed Approach

Due to the liquid crystalline character of the systems under study, a conventional unit cell cannot be found. Instead of using a representative small unit cell, we treated the whole simulation box as an effective supercell. Letting L_x, L_y and L_z define the supercell of the orthogonal simulation box and denoting the three directions of space by the unit vectors $\hat{x}, \hat{y}, \hat{z}$, the supercell vectors are given by the following equations:

$$\vec{a}_{cell} = L_x \hat{x}, \quad \vec{b}_{cell} = L_y \hat{y}, \quad \vec{c}_{cell} = L_z \hat{z} \qquad (3.22)$$

The position vector of an atom labeled with index j is expressed as:

$$\vec{r}_j = x_j \hat{x} + y_j \hat{y} + z_j \hat{z} \qquad (3.23)$$

where x_j, y_j and z_j are the coordinates of the atom indexed as j. Equivalently, using the fractional coordinates x_j', y_j' and z_j' defined as:

$$x_j' = \frac{x_j}{L_x}, y_j' = \frac{y_j}{L_y}, z_j' = \frac{z_j}{L_x} \qquad (3.24)$$

the position vector can be rewritten into:

$$\vec{r}_j = x_j' \vec{a}_{cell} + y_j' \vec{b}_{cell} + z_j' \vec{c}_{cell} \qquad (3.25)$$

The associated vectors $\vec{a}_{cell}^*$, $\vec{b}_{cell}^*$ and $\vec{c}_{cell}^*$ that span the reciprocal space are given from the equations below:

$$\vec{a}_{cell}^* = 2\pi \frac{\vec{b}_{cell} \times \vec{c}_{cell}}{\vec{a}_{cell} \cdot (\vec{b}_{cell} \times \vec{c}_{cell})}, \vec{b}_{cell}^* = 2\pi \frac{\vec{c}_{cell} \times \vec{a}_{cell}}{\vec{a}_{cell} \cdot (\vec{b}_{cell} \times \vec{c}_{cell})} \quad (3.26),(3.27)$$

$$\vec{c}_{cell}^* = 2\pi \frac{\vec{a}_{cell} \times \vec{b}_{cell}}{\vec{a}_{cell} \cdot (\vec{b}_{cell} \times \vec{c}_{cell})} \qquad (3.28)$$

In the case of an orthogonal supercell, the reciprocal vector $\vec{a}_{cell}^*$ can be calculated as:

$$\Rightarrow \vec{a}_{cell}^* = \frac{2\pi}{L_x} \hat{x}$$

$$\vec{a}_{cell}^* = 2\pi \frac{\vec{b}_{cell} \times \vec{c}_{cell}}{\vec{a}_{cell} \cdot (\vec{b}_{cell} \times \vec{c}_{cell})} = 2\pi \frac{L_y L_z (\hat{y} \times \hat{z})}{L_x L_y L_z [\hat{x} \cdot (\hat{y} \times \hat{z})]} = 2\pi \frac{\hat{x}}{L_x (\hat{x} \cdot \hat{x})} \qquad (3.29)$$

Similarly, it can be shown that $\vec{b}_{cell}^* = \frac{2\pi}{L_y} \hat{y}$ and $\vec{c}_{cell}^* = \frac{2\pi}{L_z} \hat{z}$.

It is obvious that the scalar products $\vec{a}_{cell}^* \cdot \vec{a}_{cell}, \vec{b}_{cell}^* \cdot \vec{b}_{cell}, \vec{c}_{cell}^* \cdot \vec{c}_{cell}$ are equal to 2π. Furthermore, for an orthogonal supercell, vectors $\vec{a}_{cell}^*, \vec{b}_{cell}^*, \vec{c}_{cell}^*$ are parallel to vectors $\vec{a}_{cell}, \vec{b}_{cell}, \vec{c}_{cell}$, respectively. The position vector of a (hkl) node of a mesh point of the reciprocal space can be expressed as:

$$\vec{s}_{hkl} = h\vec{a}^*_{cell} + k\vec{b}^*_{cell} + l\vec{c}^*_{cell}$$

$$\vec{s}_{hkl} = h\frac{2\pi}{L_x}\hat{x} + k\frac{2\pi}{L_y}\hat{y} + l\frac{2\pi}{L_z}\hat{z} \qquad (3.30)$$

$$\vec{s}_{hkl} = 2\pi\left(s_x\hat{x} + s_y\hat{y} + s_z\hat{z}\right)$$

where s_x, s_y and s_z are the components of $\vec{s}_{hkl}$ and h, k and l are the Miller indices. The magnitude of the position vector in the reciprocal space is equal to:

$$\left|\vec{s}_{hkl}\right| = \sqrt{4\pi^2\left(s_x^2 + s_y^2 + s_z^2\right)} = 2\pi\sqrt{\left(\frac{h}{L_x}\right)^2 + \left(\frac{k}{L_y}\right)^2 + \left(\frac{l}{L_z}\right)^2} \qquad (3.31)$$

The magnitude of the reciprocal lattice vector in the case of an orthogonal lattice is related with the spacing of an *hkl* plane in the direct space via the following formula:

$$\frac{1}{d_{hkl}} = \left|\vec{s}_{hkl}\right| \qquad (3.32)$$

As far as the atomic from factor, f, is concerned the real and imaginary part are considered explicitly.

$$f = \text{Re}(f) + i\,\text{Im}(f) \qquad (3.33)$$

The real part is expressed as:

$$\text{Re}(f) = f_0 + f_1 + f_{\text{rel}} - Z + f_{\text{NT}} \qquad (3.34)$$

The terms in the equation above are discussed below. f_0 is the non-resonant (Thomson) term given by an analytical approximation proposed by Doyle & Turner[42]. In this approximation, f_0 can be expressed as a linear combination of n Gaussians:

$$f_0\left(\frac{\vec{Q}}{4\pi}\right) = \sum_{j=1}^{n} a_j e^{-b_j\left(\frac{\vec{Q}}{4\pi}\right)^2} + c \qquad (3.35)$$

Parameters a_j, b_j and c are determined by curve fitting procedures from the work of D. Waasmaier and A. Kifrel[43] for $n=5$ (eleven parameters are used in total).

$$f_0\left(\frac{\vec{Q}}{4\pi}\right) = \sum_{j=1}^{5} a_j e^{-b_j\left(\frac{\vec{Q}}{4\pi}\right)^2} + c \qquad (3.36)$$

f_1–Z is the non-relativistic anomalous dispersion term and f_{rel} is the relativistic correction factor. Nuclear Thomson scattering of photons is the analog of the classical Thomson scattering of light by electrons. In the classical picture of this process, the nuclear charge and the center of mass of the whole nucleus oscillate in the same frequency as that of the electric field of the incident radiation. f_{NT} stands for the nuclear Thompson correction term.

As explained earlier, the form factor can be derived by treating electrons of an atom as damped harmonic oscillators. The velocity-dependent damping term represents dissipation of energy from the applied field, primarily due to re-radiation. This damping term give rise to an imaginary part of the atomic form factor which is related to the photo absorption.

As explained earlier, the structure factor arising from a molecule is:

$$F^{mol}\left(\vec{Q}\right) = \sum_{j}^{N} f_j(\vec{Q})e^{i\vec{Q}\cdot\vec{r}_j} \tag{3.37}$$

Utilizing the Laue condition for diffraction ($\vec{Q} = \vec{s}_{hkl}$), the structure factor, F_{hkl}, associated with a *hkl* node can be calculated as:

$$
\begin{aligned}
F_{hkl} &= \sum_{j} f_j \exp\left(-i\vec{r}_j \cdot \vec{s}_{hkl}\right) = \sum_{j} f_j \exp\left[-2\pi i\left(hx_j^{'} + ky_j^{'} + lz_j^{'}\right)\right] \\
&= \sum_{j}\left[\operatorname{Re}\left(f_j\right) + i\operatorname{Im}\left(f_j\right)\right]\left[\cos\left(2\pi\left(hx_j^{'} + ky_j^{'} + lz_j^{'}\right)\right) - i\sin\left(2\pi\left(hx_j^{'} + ky_j^{'} + lz_j^{'}\right)\right)\right] \\
F_{hkl} &= \sum_{j}\left[\operatorname{Re}(f)\cos\left(2\pi\left(hx_j^{'} + ky_j^{'} + lz_j^{'}\right)\right) + \operatorname{Im}(f)\sin\left(2\pi\left(hx_j^{'} + ky_j^{'} + lz_j^{'}\right)\right)\right] + \\
&\quad i\sum_{j}\left[\operatorname{Im}(f)\cos\left(2\pi\left(hx_j^{'} + ky_j^{'} + lz_j^{'}\right)\right) - \operatorname{Re}(f)\sin\left(2\pi\left(hx_j^{'} + ky_j^{'} + lz_j^{'}\right)\right)\right]
\end{aligned} \tag{3.38}
$$

where the first sum in equation 3.38 corresponds to the real part of the structure factor and the second sum to the Imaginary part.

The calculated Intensity, $I_{hkl}\left(s\right)$, for a given *hkl* node is given by the square of the norm of the structure factor:

$$I_{hkl}\left(s\right) = \left|F_{hkl}\left(s\right)\right|^2 \tag{3.39}$$

3.5 Analyzing XRD and 2D-WAXD patterns

The main purpose of this analysis is the direct comparison between experimental and computational diffractograms. Two types of widely available diffractograms have been

examined, namely X-Ray Diffraction (XRD) spectra and 2D Wide Angle X-ray Diffraction (WAXD) patterns. XRD spectra are extracted by binning the calculated intensity with respect to the magnitude of the reciprocal position vector.

In order to determine the Bravais lattice in which the molecular wires are arranged, the position of the peaks in the reciprocal space should be taken into account. Fourteen distinct families of Bravais lattices exist in three dimensions. The lattice spacing (d_{hkl}) of a given family is expressed as a function of Miller indices (h,k,l) and lattice parameters. Lattice parameters are quantified by the magnitudes (a,b,c) and the angles (α,β,γ) of the lattice vectors. The type of crystal symmetry may be revealed by changing the hkl nodes (in a trial and error manner) until the lattice spacing relation of a specific Bravais family is satisfied for all intense peaks.

WAXD patterns are calculated in two steps: first the position vector in the reciprocal space is decomposed into the $\vec{s}^{\,*}_{xy}$ and $\vec{s}^{\,*}_{z}$ terms. Afterwards, WAXD patterns are determined by binning the sum of intensities into 2D histograms with respect to the aforementioned components. The 2D WAXD pattern is spanned by two Cartesian axes, namely the equator and the meridian. The main characteristics in a 2D WAXD fiber diffraction pattern arising are discussed as follows:

Equatorial reflections

Reflections on the equator occur from X-rays diffracted by atoms which are located in the xy plane. This is the case were $h,k \neq 0$ and $l=0$. Nanographene molecular wires are arranged in a regular Bravais lattice. The relative spacing between reflections in the equator indicates the packing of those wires.

Meridian reflections

Reflections on the meridian arise from the arrangement of the disks within the molecular columns (wires). The columnar direction is perpendicular to the disk planes and coincides with the z and z^* axes in the real and reciprocal space, respectively.

Alkyl halo

The diffuse alkyl halo is arising from the liquid-like (isotropic) structure of the aliphatic side chains. Aliphatic chains are moving in a random manner, as a result of thermal motion, and give rise to a "ring" of constant intensity.

Diagonal reflections

Diagonal reflections arise from nodes with $h,k \neq 0$ and l=constant ($\neq 0$). These reflections provide information about possible helical supramolecular arrangements and more precisely about the angle between neighboring polyaromatic disks. A schematic representation of an ideal fiber diffraction pattern of a liquid crystalline material is illustrated in the figure below.
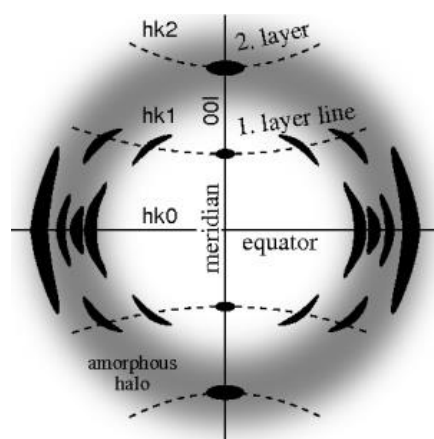

Figure 39: An ideal fiber diffraction pattern from a semi-crystalline material. The amorphous alkyl halo, arising from the isotropic character of the material, is illustrated with grey color. The intense meridian, equator and diagonal are represented with black color, alongside the associated *hkl* nodes.

3.6 Benchmarking

In order to benchmark and test the correctness of the developed computational method, a series of prototype supramolecular crystal structures have been examined. Aliphatic chains are absent from the prototype crystals. The latter are comprised from superphenalene molecules. Eight different cases have been examined: 1) A perfect crystal consisting of discotic molecules stacked perfectly within the molecular wires. 2) A perfect crystal with random columnar rotations about each wire axis. 3) A crystal in which a 20º degrees twist angle alternating pattern is applied within the molecular wires. 4) Same as 3) but with random columnar rotations. Also helical molecular wires have been examined: a 20º degrees helix 5) without and 6) with random columnar rotations and a 60º degrees helix 7) without and 8) with columnar rotations.
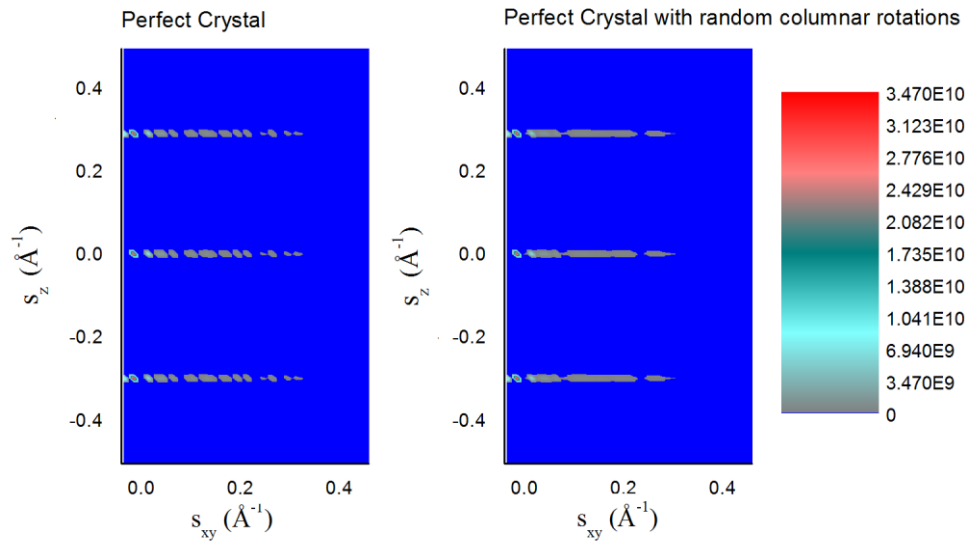
Figure 40: 2D-WAXD Left) pattern from a perfect crystal. Right) pattern from a perfect crystal with random columnar rotations.

Fiber diffraction is realized from the fact that in both cases of perfect crystals and crystals with random columnar rotation (random azimuthal orientation) the patterns are the same. The intense reflections on the meridian ($0.025Å^{-1}$, $0.047Å^{-1}$), ($-0.020Å^{-1}$, $-02980Å^{-1}$) and ($0.020Å^{-1}$, $02980Å^{-1}$) are evident and arise from neighboring aromatic disks which stack due to π-π interactions between the aromatic cores. The reflections on the equator arise from neighboring molecular wires.
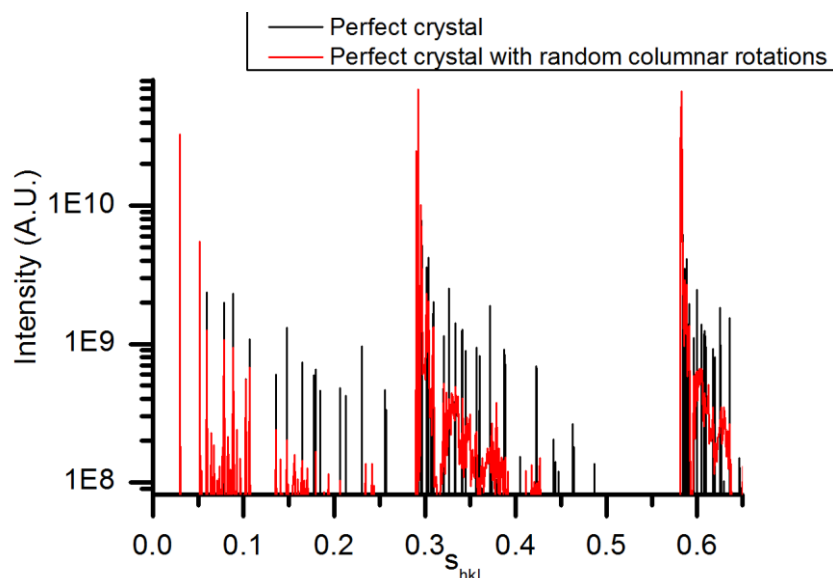
Figure 41. XRD pattern of perfect crystal (black) and perfect crystal with random columnar rotations (red).

In the case of perfect crystals, the peaks are sharp and arise from the perfectly aligned suparamolecular organization. In the case of perfect crystals with random columnar rotations, the peaks between 0.3-0.45 Å^{-1} and in the region of 0.6Å^{-1} are not as sharp as in the case of a perfect crystal. The rotations of the columns give rise to Bragg reflections from a wider range of distances in the reciprocal space.
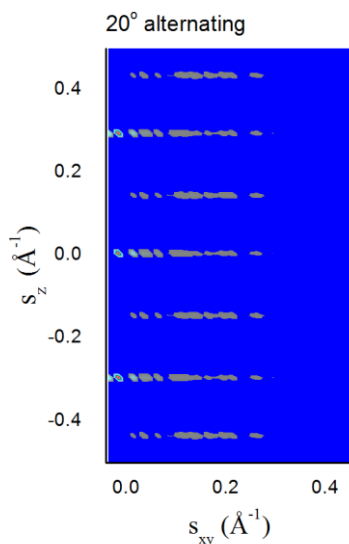

Figure 42: 2D-WAXD from a crystal with a 20 degrees alternating pattern between the disks.

Figure 43: 2D-WAXD from a crystal with a 20 degrees alternating pattern between the disks and random columnar rotations of the molecular wires.
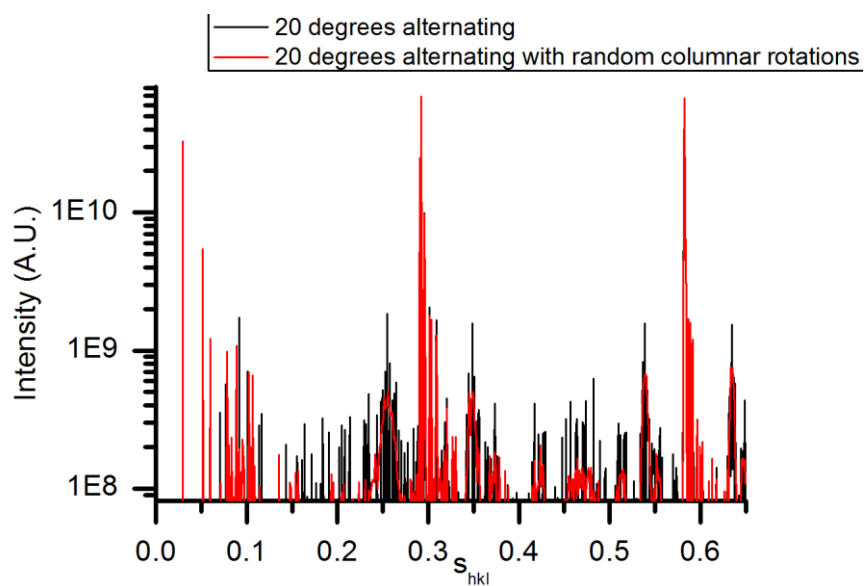
Figure 44: Figure 45. XRD pattern 20 degrees alternating (black) and 20° degrees alternating crystal with random columnar rotations (red).

Figure 46: Left) Crystal in which a 20 degrees helix is formed between the disks. Right) Crystal in which a 20 degrees helix is formed between the disks and the molecular wires are rotated in a random manner.
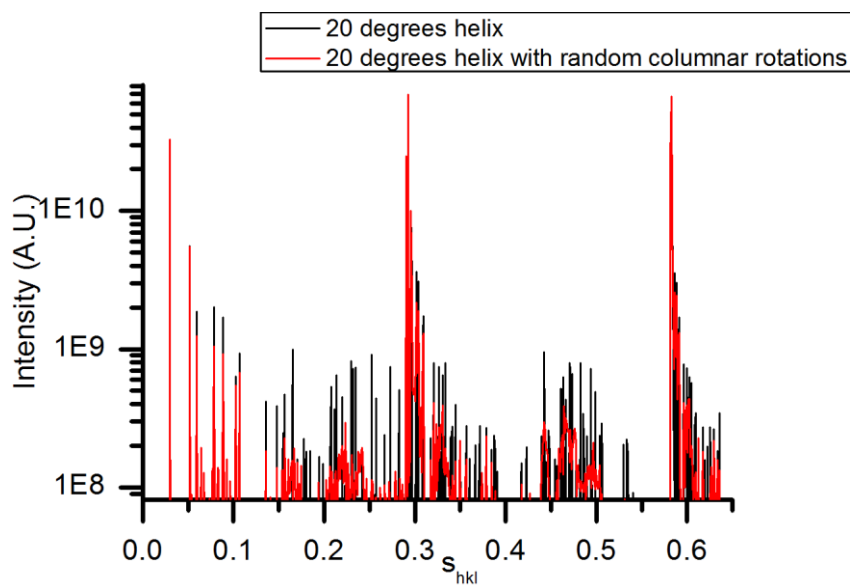
Figure 47: XRD pattern 20 degrees helix (black) and 20 degrees helical crystal with random columnar rotations (red).
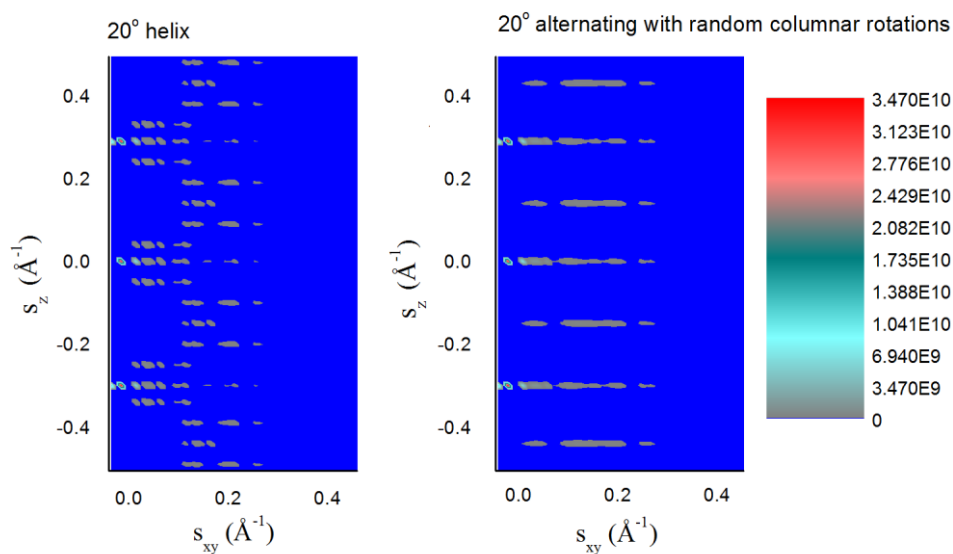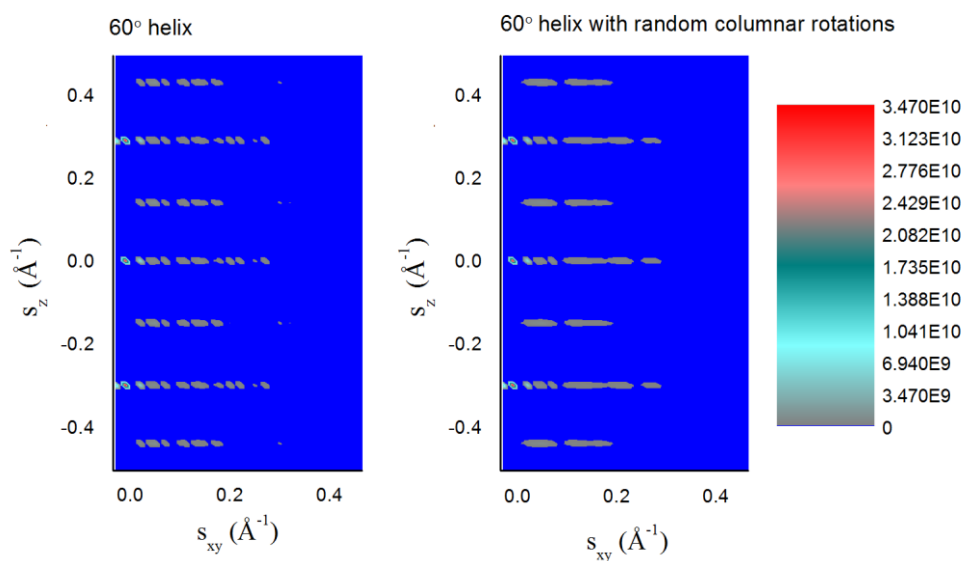

Figure 48: Left) Crystal in which a 60 degrees helix is formed between the disks. Right) Crystal in which a 60 degrees helix is formed between the disks and the molecular wires are rotated in a random manner.
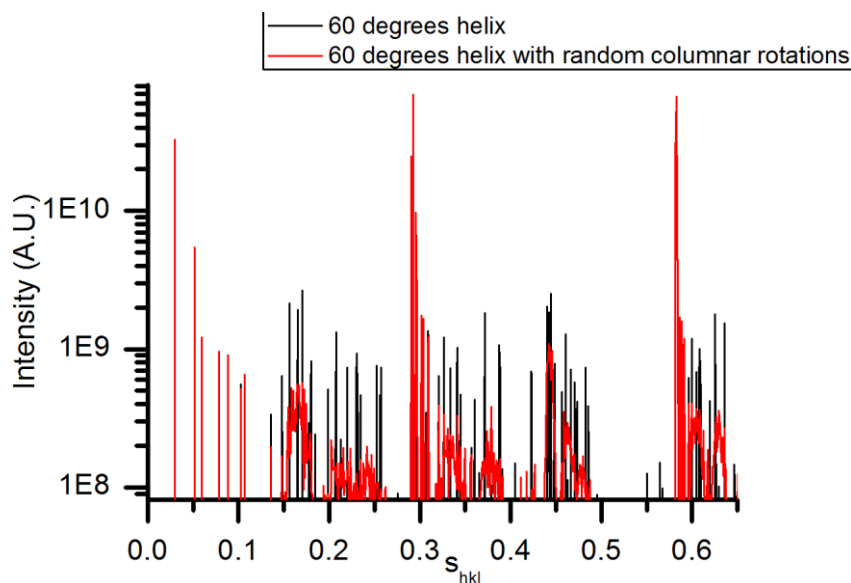
Figure 49: XRD pattern 60 degrees helix (black) and 60 degrees helical crystal with random columnar rotations (red).

3.5. Results and Discussion

3.5.1. Analysis of C96 molecular structures

Molecular crystals of superphenalene grafted with two different types of side chains, namely n-dodecane and phytyl groups, have been examined. Discotic molecules in both systems form a 20° helix. XRD and 2D-WAXD patterns were calculated from equilibrium MD trajectories at 300K and 400K.
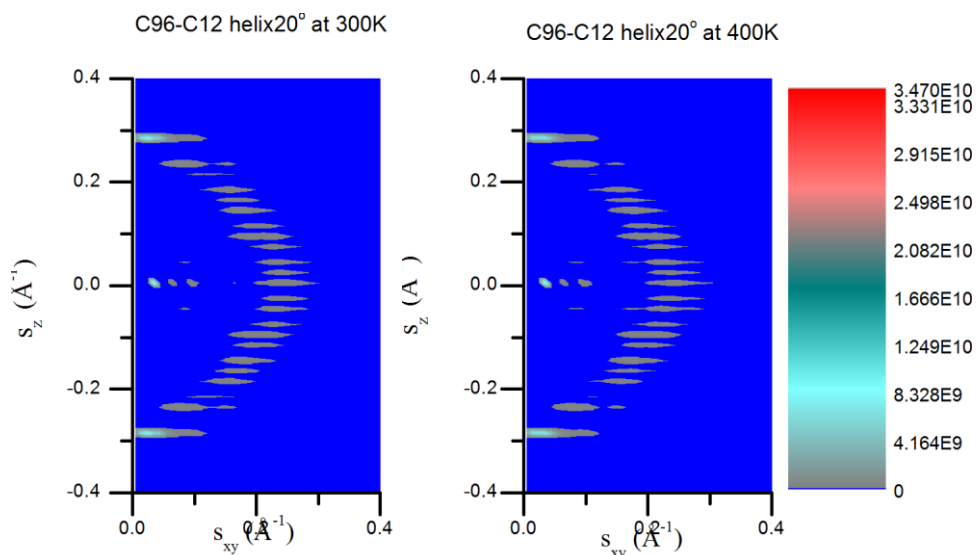
Figure 50: 2D-WAXD pattern of C96-C12 20° helix at 300K and 400K.
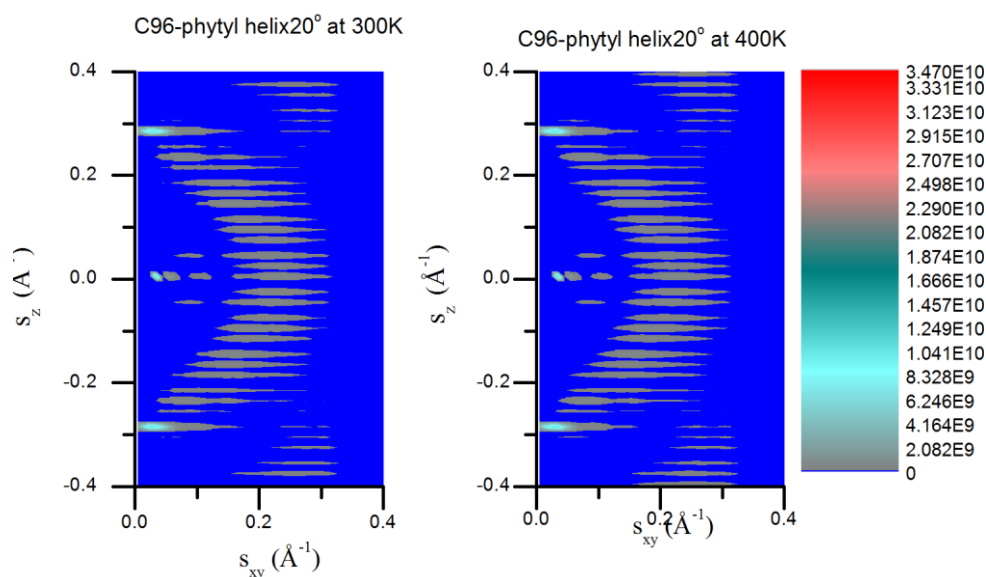
Figure 51: 2D-WAXD pattern of C96-phytyl 20° helix at 300K and 400K.
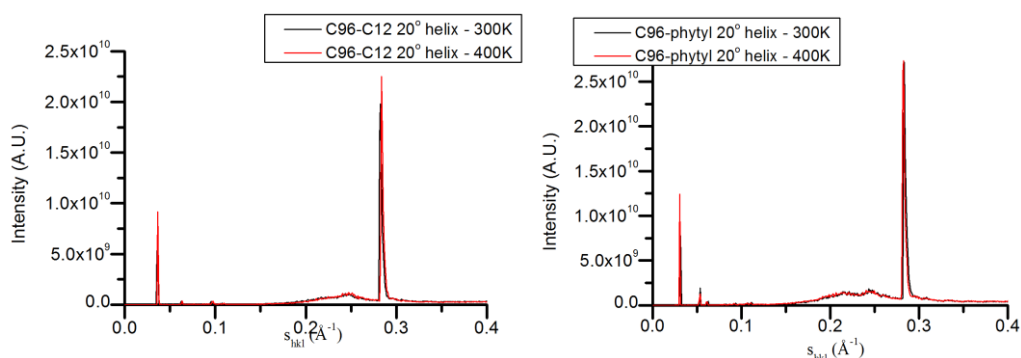
Figure 52: Left) Integrated XRD pattern of C96-C12 20° helix at 300K and 400K. Right) Integrated XRD pattern of C96-phytyl 20° helix at 300K and 400K.

The main features of a 2D-WAXD pattern are discussed as follows. The three peaks on the equator indicate the intermolecular distance between neighboring wires. The two symmetric peaks on the meridian arise from π-π stacking between polyaromatic cores. The amorphous halo that appears as a ring in the pattern is arising from the melt-like structure of the aliphatic side chains.

The case of a hexagonal lattice will be analyzed. For a given molecular wire as a reference column, the first neighboring column is located at a constant distance a. The second further column is at a distance $\sqrt{3}a$ and the third neighboring column at a distance $\sqrt{4}a = 2a$ away from the reference column. Consequently, relative reciprocal spacings between reflections on the equator will be $1, \sqrt{3}, \sqrt{4} = 2$. Furthermorere, reflections on the meridian with (h, k=0)

51

are due to the neighboring aromatic cores. Results are in good agreement with available experimental data[9,10].

In the 1D-XRD spectra of C96- phytyl 20 degrees helix system the first three peaks are located at 0.0311, 0.0537, 0.0614 with relative distances at the reciprocal space equal to 1, 1.726688103, 1.974276527. This sequence indicates the formation of a hexagonal lattice. The three peaks can labeled as 100, 110, 210, respectively.
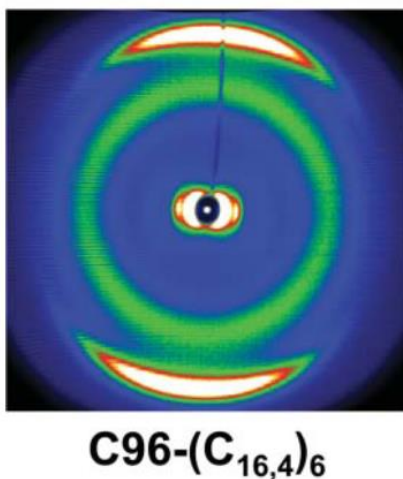
$C96-(C_{16,4})_6$

Figure 53 Experimental pattern of C96-(C$_{16,4}$)$_6$

In experimental patterns the alkyl halo arising from the phytyl groups is broader than the one arising from the dodecane groups. In addition, the theoretical patterns of C96-phytyl molecules show a wider halo in comparison with the WAXD patterns from C96-C12 molecules.

3.5.2. Analysis of C132 molecular structures

XRD and 2D-WAXD patterns are calculated for C132 molecules grafted with phytyl groups. Three different stacking profiles have been examined: a 20° helix pattern, a 90° alternating pattern and a mixed stacking pattern. Diffractograms have been extracted for 300K and 400K.[35]
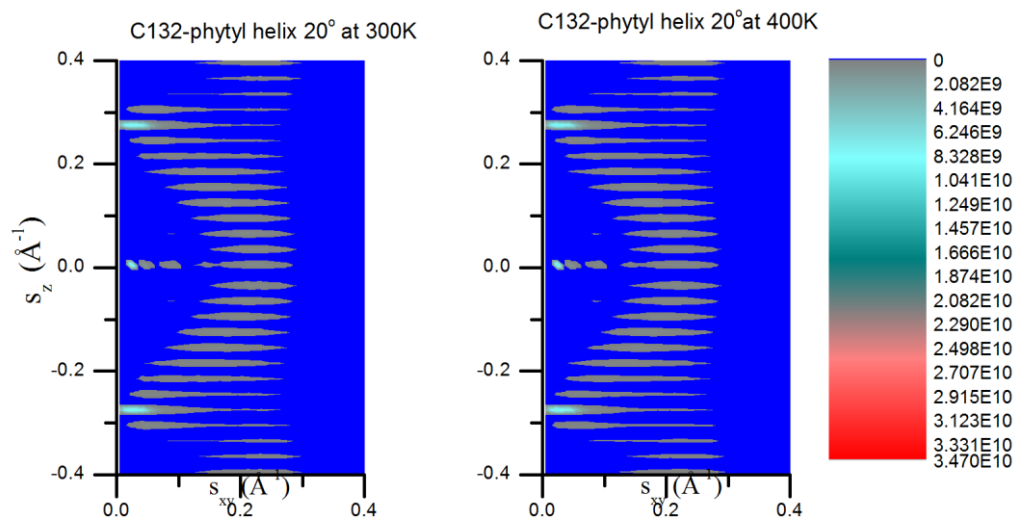
Figure 54: 2D-WAXD of C132-phytyl helix 20° system: left) 300K; right) 400K.
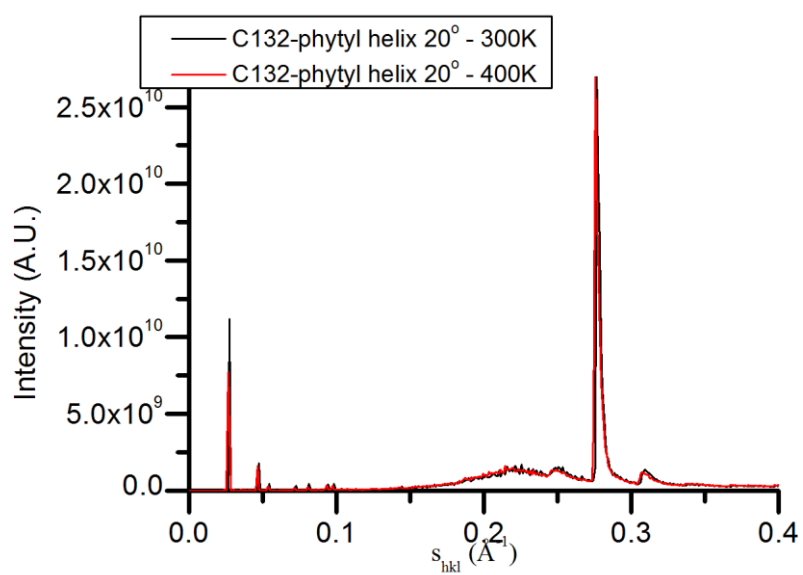
Figure 55: Integrated XRD pattern of C132-phytyl 20° helix at 300K and 400K.
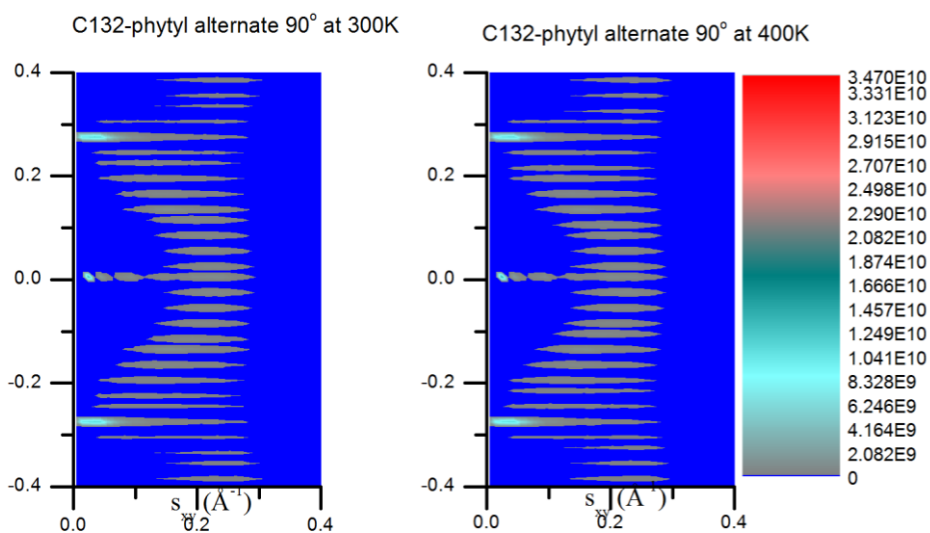
Figure 56: 2D-WAXD of C132-phytyl alternate 90° system: left) 300K; right) 400K.
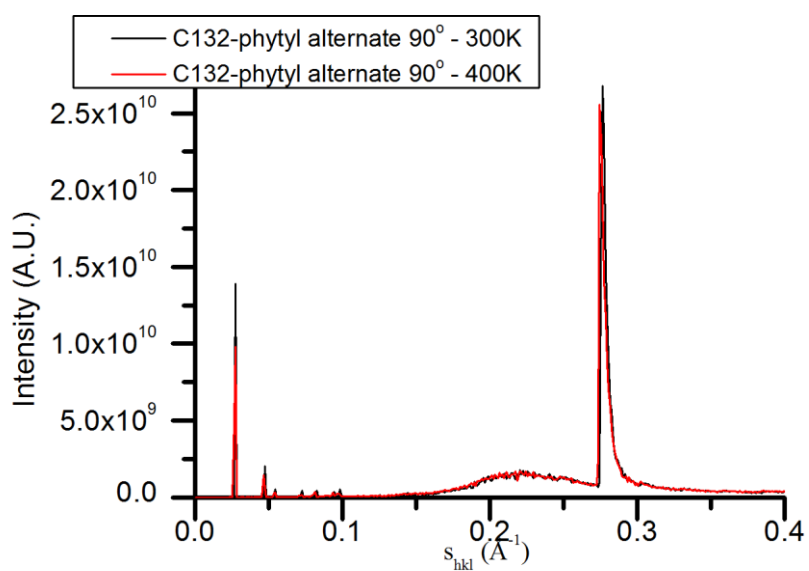
Figure 57: Integrated XRD pattern of C132-phytyl alternate 90° at 300K and 400K.
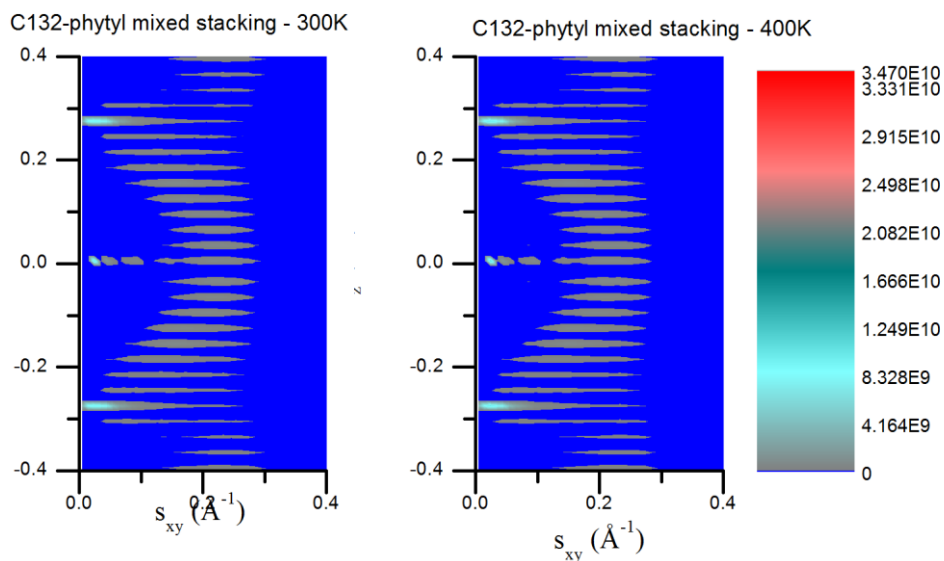
Figure 58: 2D-WAXD of C132-phytyl mixed stacking system left) 300K right) 400K
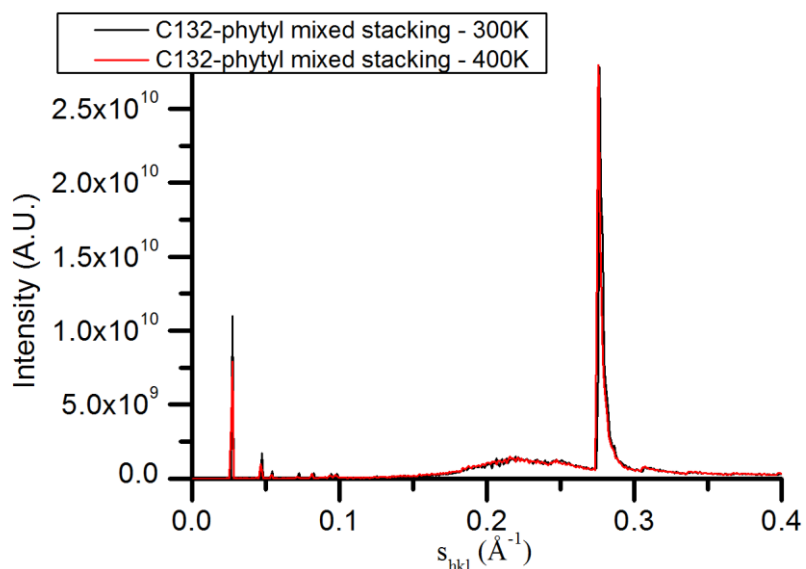
Figure 59: Integrated XRD pattern of C132-phytyl mixed stacking at 300K and 400K.
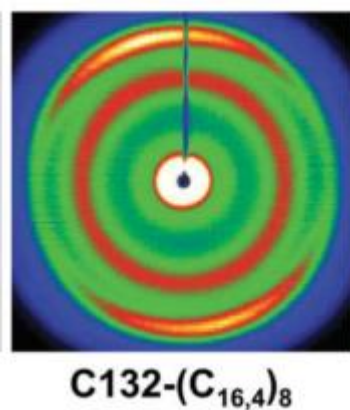
Figure 60: Experimental pattern of C132-(C$_{16,4}$)$_8$

Equatorial reflections are not visible in experimental WAXD patterns of C132-phytyl systems. Additionally, the reflections located at symmetric position at the meridian show a tilt with respect to the vertical direction.

Chapter 4: Conclusions

Nanographene liquid crystals are an interesting case study in the field of computational soft matter. An analysis from the dimer level towards molecular wire and up to molecular crystals has been carried out for discotics molecules grafted with aliphatic and phytyl side chains.

The preferable stacking patterns were determined by performing energy minimizations on a variety of dimer conformations utilizing a hybrid all-atom/united-atom force field and a second generation force field. Both empirical force fields indicate the same dimer stacking patterns which are in good agreement with available experimental data. Simulations of molecular wires and crystals were employed utilizing the first force field mentioned above, as it is sufficiently accurate and requires less computational resources.

The mobility of the attached side chains was revealed by calculating the autocorrelation function of the 2nd order Legendre polynomial for the end-to-end vector, which is the vector connecting a linking aromatic carbon and the final carbon atom of the attached side chain. From this analysis we conclude that C12 side chains tend to pack about the core wire in a neat manner, while phytyl groups are more disorganized and exhibit more pronounced thermal motion.

The information from dimer studies to single molecule wires is used in order to create initial configurations with plausible structures that are subsequently equilibrated via MD simulations. These equilibrated MD trajectories are the cornerstone of the structural XRD analyses carried out in the second part of this thesis.

In the second part of the master thesis, complete structural characterization of supramolecular nanographene liquid crystals has been carried out utilizing the principles of X-ray diffraction. In-house software was developed utilizing parallel MPI architecture in order to calculate theoretical XRD spectra. Having at hand the full scattering information of nodes in reciprocal space, simulated 2D WAXS patterns were created. Integrated theoretical XRD patterns reveal the intra- and inter-molecular arrangement by correlating the position (or angle) of the peaks with the associated lattice spacing types of relative unit-cells. Furthermore, 2D-WAXD provides additional information about structure, such as helicity and tilting. The advantage of 2D-WAXD is that the patterns arising from computational studies can be directly compared with experimental data from the literature.

This current study integrates a series of computational methods, procedures and tools aiming to a sophisticated bottom-to-top approach for the theoretical construction of discotic liquid crystalline systems, linking properties from the single molecule level to experimentally accessible structural data.

Chapter 5: Future work

Examination of different types of attached side chains is a future research plan. Grafting metallic or halogen groups can readily enhance the properties of disk-like liquid crystalline materials as compounds for organic electronic applications. Furthermore, determining the properties of molecular systems consisting of PAH of different size and symmetry is an interesting unexplored topic.

Investigation of 2D-WAXD patterns arising from triclinic simulation cells is a possible topic for future research. Extraction of patterns from other materials, such as crystalline structures, nanocomposites or amorphous polymers close to the glass transition temperature and other types of liquid crystals is straightforward.

Acknowledgements in Greek language – Ευχαριστίες

Η παρούσα Μεταπτυχιακή Εργασία εκπονήθηκε στο εργαστήριο Υπολογιστικής Επιστήμης και Τεχνικής των Υλικών, το οποίο διευθύνεται από τον καθηγητή Θεόδωρο Ν. Θεοδώρου.

Θα ήθελα να εκφράσω τις ειλικρινέστερες ευχαριστίες μου στον επιβλέποντα καθηγητή Θεόδωρο Ν. Θεοδώρου. Σε όλη τη διάρκεια των σπουδών μου αποτέλεσε πρότυπο για μένα τόσο ως επιστήμονα για τις γνώσεις του, όσο και ως ανθρώπου για το ήθος και τις αξίες του. Τον ευχαριστώ επίσης, για τις συμβουλές που μου έδωσε, οι οποίες συντέλεσαν καταλυτικά στο να πάρω σημαντικές αποφάσεις στη ζωή μου.

Ευχαριστώ τον αναπληρωτή καθηγητή Λ. Τσέτσερη που με εισήγαγε στον κόσμο της κβαντικής μηχανικής και τον καθηγητή Κ. Χαριτίδη που δέχθηκε να με αποτελέσει μέλος της εξεταστικής μου εππιτροπής.

Επιπρόσθετα, θα ήθελα να ευχαριστήσω από καρδιάς τον υποψήφιο διδάκτορα Ορέστη Γ. Ζιώγο, ο οποίος συνεπέβλεψε τη δουλειά μου. Ο Ορέστης συνέβαλλε καταλυτικά στην εξέλιξη της ακαδημαϊκής μου πορείας. Τον ευχαριστώ θερμά, για το χρόνο που μου αφιέρωσε και για τις γνώσεις που μου μετέφερε.

Θα ήθελα να ευχαριστήσω θερμά τον Σπύρο Κουρνόπουλο για τη βοήθεια που μου παρείχε τόσο στην προπτυχιακή όσο και στη μεταπτυχιακή μου εργασία. Επίσης ευχαριστώ τον υποψήφιο διδάκτορα Άκη Τζούνη για τις πολύτιμες συμβουλές που σχετικά με το πεδίο δυνάμεων COMPASS, καθώς και τον Χρήστο Μπάρδα και Γεώργιο Κίσσα για τις όμορφες στιγμές εντός και εκτός εργαστηρίου. Ευχαριστώ τη Μαρίνα για τις ώρες που διαβάζαμε παρέα κβαντική στο πρώτο έτος του μεταπτυχιακού και την Αλεξάνδρα για τις ευχάριστες στιγμές στην Κρήτη .

Παράλληλα θα ήθελα να ευχαριστήσω τα μέλη του εργαστηρίου Υπολογιστικής Επιστήμης και Τεχνικής των Υλικών με τα οποία μοιραστήκαμε ευχάριστες στιγμές στο εργαστήριο και ήταν πάντα πρόθυμοι να βοηθήσουν. Τέλος ευχαριστώ τη μητέρα μου για την υποστήριξή της σε όλα τα επίπεδα.

Bibliography

(1)   Kumar, S. Self-Organization of Disc-like Molecules: Chemical Aspects. *Chem. Soc. Rev.* **2006**, *35*, 83–109.

(2)   Muller, S.; Mullen, K. Expanding Benzene to Giant Graphenes: Towards Molecular Devices. *Philos. Trans. R. Soc. A Math. Phys. Eng. Sci.* **2007**, *365*, 1453–1472.

(3)   Wong, W. W. Polycyclic Aromatic Hydrocarbons for Organic Photovoltaics. **2011**, *8312*, 83120J.

(4)   Wu, J.; Pisula, W.; Mullen, K. Graphenes as Potential Material for Electronics. *Chem. Rev.* **2007**, *107*, 718–747.

(5)   Van De Craats, A. M.; Warman, J. M. Core-Size Effect on the Mobility of Charge in Discotic Liquid Crystalline Materials. *Adv. Mater.* **2001**, *13*, 130–133.

(6)   Fischbach, I.; Pakula, T.; Minkin, P.; Fechtenkötter, A.; Müllen, K.; Spiess, H. W.; Saalwächter, K. Structure and Dynamics in Columnar Discotic Materials: A Combined X-Ray and Solid-State NMR Study of Hexabenzocoronene Derivatives. *J. Phys. Chem. B* **2002**, *106*, 6408–6418.

(7)   Ziogos, O. G.; Theodorou, D. N. Molecular Dynamics Simulations of Alkyl Substituted Nanographene Crystals. *Mol. Phys.* **2015**, *113*, 2776–2790.

(8)   Müllen, K.; Rabe, J. P. Nanographenes as Active Components of Single-Molecule Electronics and How a Scanning Tunneling Microscope Puts Them to Work. *Acc. Chem. Res.* **2008**, *41*, 511–520.

(9)   Tomović, Ž.; Watson, M. D.; Müllen, K. Superphenalene-Based Columnar Liquid Crystals. *Angew. Chemie - Int. Ed.* **2004**, *43*, 755–758.

(10)   Pisula, W.; Tomović, Ž.; Simpson, C.; Kastler, M.; Pakula, T.; Müllen, K. Relationship between Core Size, Side Chain Length, and the Supramolecular Organization of Polycyclic Aromatic Hydrocarbons. *Chem. Mater.* **2005**, *17*, 4296–4303.

(11)   Press, W. H.; Teukolsky, S. A.; Vetterling, W. T.; Flannery, B. P. *NUMERICAL RECIPES The Art of Scientific Computing*; 3rd ed.; Cambridge University Press: New York, 2007.

(12)   Powell, M. J. D. Restart Procedures for the Conjugate Gradient Method. *Math. Program.* **1977**, *12*, 241–254.

(13)   Theodorou, D. N. *Applied Molecular Theory for Engineers*; Athens, 2004.

(14)   Alen, M. P.; Tildesley, D. J. *Computer Simulations of Liquids*; Oxford University Press: New York, 1991.

(15)   Frenkel, D.; Berend, S. *Understanding Molecular Simulation - From Algorithms to Applications*; 2nd ed.; Academic Press, 2002.

(16)   Beeman, D. Some Multistep Methods for Use in Molecular Dynamics Calculations. *J. Comput. Phys.* **1976**, *20*, 130–139.

(17)   Berendsen, H. J. C.; Postma, J. P. M.; van Gunsteren, W. F.; DiNola, A.; Haak, J. R. Molecular Dynamics with Coupling to an External Bath. *J. Chem. Phys.* **1984**, *81*, 3684–3690.

(18)   Evans, D. J.; Holian, B. L. The Nose–Hoover Thermostat. *J. Chem. Phys.* **1985**, *83*, 4069–4074.

(19)   Martyna, G. J.; Tobias, D. J.; Klein, M. L. Constant Pressure Molecular Dynamics Algorithms. *J. Chem. Phys.* **1994**, *101*, 4177–4189.

(20)   Parrinello, M.; Rahman, A. Polymorphic Transitions in Single Crystals: A New Molecular Dynamics Method. *J. Appl. Phys.* **1981**, *52*, 7182–7190.

(21)   Sun, H. COMPASS: An Ab Initio Force-Field Optimized for Condensed-Phase Applications-Overview with Details on Alkane and Benzene Compounds. *J. Phys. Chem. B* **1998**, *102*, 7338–7364.

(22)   Wang, J.; Wolf, R. M.; Caldwell, J. W.; Kollman, P. A.; Case, D. A. Development and Testing of a General Amber Force Field. *J Comput Chem* **2004**, *25*, 1157–1174.

(23)   Jorgensen, W. L.; Madura, J. D.; Swenson, C. J. Optimized Intermolecular Potential Functions for Liquid Hydrocarbons. *J. Am. Chem. Soc.* **1984**, *106*, 6638–6646.

(24)   Jorgensen, W. L.; Severance, D. L. Aromatic-Aromatic Interactions: Free Energy Profiles for the Benzene Dimer in Water, Chloroform, and Liquid Benzene. *J. Am. Chem. Soc.* **1990**, *112*, 4768–4774.

(25)   Marcon, V.; Breiby, D. W.; Pisula, W.; Dahl, J.; Kirkpatrick, J.; Patwardhan, S.; Grozema, F.; Andrienko, D. Understanding Structure-Mobility Relations for Perylene Tetracarboxydiimide Derivatives. *J. Am. Chem. Soc.* **2009**, *131*, 11426–11432.

(26)   Plimpton, S. Fast Parallel Algorithms for Short – Range Molecular Dynamics. *J. Comput. Phys.* **1995**, *117*, 1–19.

(27)   Hockney, R. W.; Eastwood, J. W. *Computer Simulation Using Particles*; Adam Hilger: New York, 1989.

(28)   Yu, W.; He, X.; Vanommeslaeghe, K.; Mackerell, A. D. Extension of the CHARMM General Force Field to Sulfonyl-Containing Compounds and Its Utility in Biomolecular Simulations. **2012**.

(29)   Vanommeslaeghe, K.; Hatcher, E.; Acharya, C.; Kundu, S.; Zhong, S.; Shim, J.; Darian, E. CHARMM General Force Field : A Force Field for Drug-Like Molecules Compatible with the CHARMM All-Atom Additive Biological Force Fields. **2009**.

(30)   Theodorou, D. N.; Suter, U. W. Molecular Structure of Vinyl Polymer Glass. *Am. Chem. Soc. Polym. Prepr. Div. Polym. Chem.* **1984**, *25*, 180.

(31)   Als-Nielsen, J.; McMorrow, D. *Elements of Modern X-Ray Physics*; 2nd ed.; John Wiley & Sons, Ltd Publication: United Kingdom, 2011.

(32)   C.Kittel. *Introduction to Solid State Physics*; 8th ed.; John Wiley & Sons, Ltd Publication: United States, 2005.

(33)   Economou, E. N. *The Physics of Solids- Essentials and Beyond*; Springer, 2010.

(34)   Simpson, C. D.; Wu, J.; Watson, M. D.; Müllen, K. From Graphite Molecules to Columnar Superstructures – an Exercise in Nanoscience. *J. Mater. Chem.* **2004**, *14*, 494–504.

(35)   Tomović, Ž. New Discotic Liquid Crystals Based on Large Polycyclic Aromatic Hydrocarbons as Materials for Molecular Electronics, Johannes Gutenberg-Universität Mainz, 2004.

(36)   Breiby, D. W.; Lemke, H. T.; Hammershøj, P.; Andreasen, J. W.; Nielsen, M. M. X-Ray Diffraction Study of Directionally Grown Perylene Crystallites. *J. Phys. Chem. C* **2008**, *112*, 4569–4572.

(37)   Breiby, D. W.; Bunk, O.; Andreasen, J. W.; Lemke, H. T.; Nielsen, M. M. Simulating X-Ray Diffraction of Textured Films. *J. Appl. Crystallogr.* **2008**, *41*, 262–271.

(38)   Mao, Y.; Li, X.; Burger, C.; Hsiao, B. S.; Mehta, A. K.; Tsou, A. H. Structure Development during Stretching and Heating of Isotactic Propylene-1-Butylene Random Copolymer: From Unit Cells to Lamellae. *Macromolecules* **2012**, *45*, 7061–7071.

(39)   Mao, Y.; Burger, C.; Li, X.; Hsiao, B. S.; Mehta, A. K.; Tsou, A. H. Time-Resolved Synchrotron X-Ray Scattering Study on Propylene-1-Butylene Random Copolymer Subjected to Uniaxial Stretching at High Temperatures. *Macromolecules* **2012**, *45*, 951–961.

(40)   Cho, E.; Risko, C.; Kim, D.; Gysel, R.; Cates Miller, N.; Breiby, D. W.; McGehee, M. D.; Toney, M. F.; Kline, R. J.; Bredas, J. L. Three-Dimensional Packing Structure and Electronic Properties of Biaxially Oriented poly(2,5-bis(3-Alkylthiophene-2-yl)thieno[3,2- B]Thiophene) Films. *J. Am. Chem. Soc.* **2012**, *134*, 6177–6190.

(41)   Mao, Y.; Burger, C.; Zuo, F.; Hsiao, B. S.; Mehta, A.; Mitchell, C.; Tsou, A. H. Wide-Angle X-Ray Scattering Study on Shear-Induced Crystallization of Propylene-1-Butylene Random Copolymer: Experiment and Diffraction Pattern Simulation. *Macromolecules* **2011**, *44*, 558–565.

(42)   Doyle, P. A.; Turner, P. S. Relativistic Hartree–Fock X-Ray and Electron Scattering Factors. *Acta Crystallogr. Sect. A* **1968**, *24*, 390–397.

(43)   Waasmaier, D.; Kirfel, A. New Analytical Scattering-Factor Functions for Free Atoms and Ions. *Acta Crystallogr. Sect. A* **1995**, *51*, 416–431.